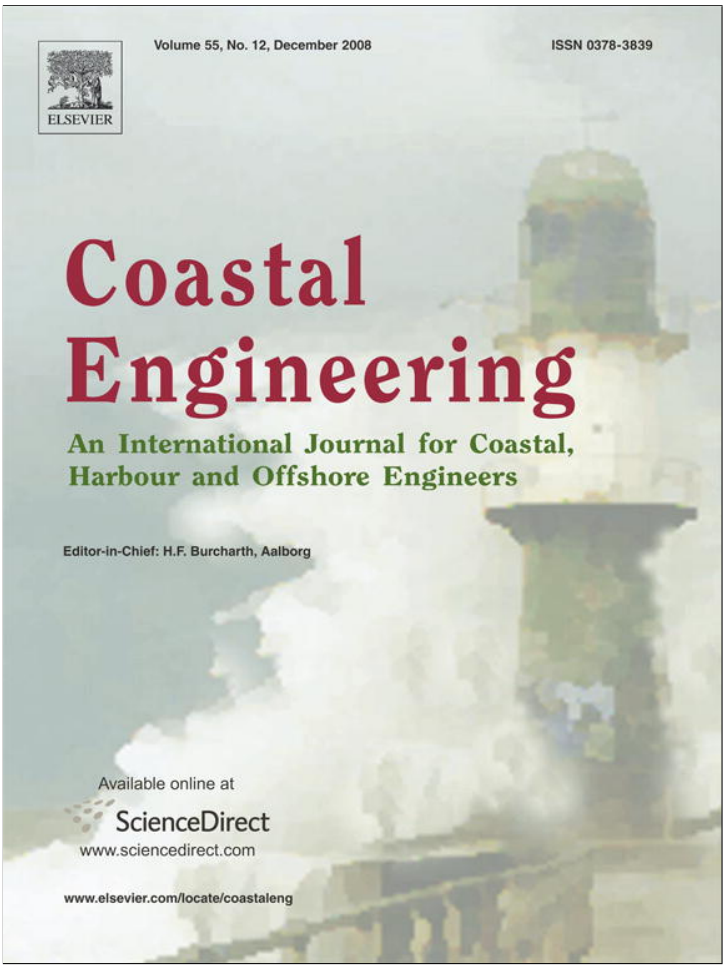

Coastal Engineering 55 (2008) 989–1004

Contents lists available at ScienceDirect

Coastal Engineering

journal homepage: www.elsevier.com/locate/coastaleng

Laboratory investigations on impulsive waves caused by underwater landslide

B. Ataie-Ashtiani *, A. Najafi-Jilani

Department of Civil Engineering, Sharif University of Technology, Tehran, Iran

ARTICLE INFO

Article history:
Received 16 September 2007
Received in revised form 1 March 2008
Accepted 12 March 2008
Available online 28 April 2008

Keywords:
Impulsive waves
Underwater landslide
Wave energy
Wave nonlinearity
Deforming slide
Rigid slide
Laboratory measurements

ABSTRACT

Laboratory investigations have been performed on the submarine landslide generated waves by performing 120 laboratory tests. Both rigid and deforming-slide masses are considered. The effects of bed slope angle, initial submergence, slide geometry, shape and deformation on impulse wave characteristics have been inspected. Impulse wave amplitude, period, energy and nonlinearity are studied in this work. The effects of bed slope angle on energy conversion from slide into wave are also investigated. Laboratory-based prediction equations are presented for impulse wave amplitude and period in near and far-field and are successfully verified using the available data in previous laboratory and numerical works.

1. Introduction

Impulsive waves may be generated by underwater earthquakes, submarine landslides, rockslides or volcano explosions. Giant submerged landslides, normally in the form of debris avalanches, can produce impulsive waves and affect the entire coastline. Investigation on the impulse wave characteristics in near and far-field is of high importance in coastal engineering. The laboratory experiments can be considered as the most reliable and possible methods to investigate the impulse wave caused by underwater landslides. The conducted laboratory works can be classified in four categories based on the method that landslides were modeled: sub-aerial landslides considered as rigid sliding block, sub-aerial slide modeled as deformable sliding mass, underwater landslide modeled as solid block, and deformable submarine failure mass. An overview of the main experimental works in this regards are presented in Table 1.

As it can be seen in Table 1, although the sub-aerial landslide generated wave has been properly investigated using laboratory models, but there are basic distinctions between sub-aerial and underwater slide waves. The differences can be identified in wave feature as well as basic effective parameters. For sub-aerial landslides, some parameters such as slide impact velocity have an important influence on the characteristics of the impulse waves (Walder et al., 2003; Fritz et al., 2004; Panizzo et al., 2005; Ataie-Ashtiani and Malek-Mohammadi, 2007). However, other parameters such as initial submergence are important for underwater landslide generated waves. Regarding underwater landslide waves, some experimental investigations were performed by Heinrich (1992) and Rzadkiewicz et al. (1997) and Ataie-Ashtiani and Shobeyri (2008) used the data for verification of their numerical model. Watts (1998) presented some laboratory works on impulse waves caused by underwater slide. The experiments were performed only over 45° bed slope with triangular rigid slide. Enet et al. (2003), and Grilli and Watts (2005) carried out some experimental works in three-dimensional wave tank. The bed slope angle was fixed on 15° and slide was modeled as a fixed semi-elliptical rigid slide. They used the experimental data to verify their well-validated numerical model (BIEM). They also presented some numerical-based prediction equations only for impulse wave amplitude in near-field.

The main objectives of this work are to provide laboratory data covering some of the obscure and limitations of the previous works. A large number of laboratory tests are performed. The effects of bed slope angle on wave are investigated in a wide range as 15 to 60 . Impulse wave characteristics such as amplitude, period, energy and nonlinearity are considered and studied in this work. The effects of bed slope angle on energy conversion from slide into wave are also investigated. Also, the effect of slide deforming and shape on impulse wave characteristics is inspected. Finally, laboratory-based forecasting equations are presented for impulse wave amplitude and period in near and far-field and they are verified using available data from previous laboratory and numerical works.

2. Experimental set-up[1]

Experiments were set-up in a 2.5 m wide, 1.8 m deep and 25 m long wave tank at Sharif University of Technology, Iran. The experimental

* Corresponding author. Fax: +98 21 66014828.
E-mail address: ataie@sharif.edu (B. Ataie-Ashtiani).

[1] Full information about experimental set-up including tabulated data, pictures and movies are presented on http://civil.sharif.edu/~ataie/ImpWave/SubmarinExp.

0378-3839/$ – see front matter © 2008 Elsevier B.V. All rights reserved.
doi:10.1016/j.coastaleng.2008.03.003

Table 1
Literature review on landslide generated waves; comparison and categorization

References	Tank dimensions			Bed slope (degree)	Failure mass specifications	Model dimensions	Wave stage
	L (m)	*W* (m)	*H* (m)				
Category 1: sub-aerial landslides considered as rigid sliding block							
Johnson and Bermel (1949)	Shallow water tank			–	Steel plate	–	G
Wiegel (1955)	Shallow water tank			–	Steel plate	–	G
Prins (1958)	Shallow water tank			–	Steel plate	–	G
Kamphuis and Bowering (1972)	Shallow water tank			45	Steel box	–	G
Heinrich (1992)	4.0	0.3	2.0	45, 30	Triangle solid block (50×50 cm)	2VD	G
Walder et al. (2003)	3.0	0.285	1.0	10 20	Hollow rectangular nylon box	2VD	G
Panizzo et al. (2005)	11.5	6	0.8	16 36	Solid rectangular box	3D	G, P, R
Category 2: sub-aerial slide modeled as deformable sliding mass							
Fritz et al. (2004)	11	0.5	1.0	45	Failure soil mass caused by PLG	2VD	G, P
Category 3: underwater landslide modeled as solid block							
Watts (1998)	9.14	0.101	0.66	45	PVC triangle-section (86×86 mm)	2VD	G
Grilli and Watts (2005)	30	3.6	1.8	15	Semi-ellipse aluminum sheet	2VD	G, P
Enet et al. (2003)	30	3.6	1.8	15	Semi-ellipse aluminum sheet	3D	G, P
Category 4: deformable submarine failure mass							
Heinrich (1992)	4.0	0.3	2.0	30, 45	Gravel with identical diameter	2VD	G
Watts et al. (2003)	30	3.6	1.8	45	Glass beads, steel shots and lead shots	2VD	G

2VD: Two-vertical dimensional; G: Generation of impulse wave; 3D: Three dimensional; P: Propagation of impulse wave; PLG: Pneumatic landslide generator; R: Run-up of impulse wave.

set-up included two inclined planes with adjustable slope between 15 and 60 . One of the inclined beds was made for sliding down solid blocks and another one for observation of run-up of slide-generated waves. The sliding surface was smooth and was also lubricated in order to provide a frictionless slope. Therefore, the blocks could slide freely on the slope. A schematic of the wave tank and the adjustable slopes are shown in Fig. 1.

There were transparent windows at the tank wall for observation of the free water surface profile. Waves were generated by sliding down solid blocks along on the inclined bed. The blocks had different shape, volume and thickness and they had been made of steel plate with 2 mm thickness. All of the specifications of rigid blocks are given in Table 2. The total weight of block was determined based on the weight of steel plates and the filling water weight. It was considered that the block was full of water. Fig. 2 shows the schematics of rigid blocks. The water surface fluctuations were measured in eight points located at the central axis of the tank using Validyne DP15 differential pressure transducers (DPD-DP15). The locations of wave gauges ST1 to ST8 are shown on Fig. 1. All of the specifications of wave gauges are listed in Table 3.

Transducers used in hydraulic transient studies must have a fast response to the changes of pressure. Validyne variable reluctance sensors used here have only a single moving part, the sensing diaphragm. The diaphragm is free to move quickly as the pressure changes; there are no linkages or other mechanical connections to slow the sensor down. Additionally, variable reluctance sensors have extremely small displacement volumes. The DP15 series need just 6.0E–4 $in.^3$ (9.8 mm^3) of fluid to go from 0 to full scale reading. The combination of small displacement volume and only a single moving part makes the variable reluctance sensor ideal for measuring rapidly changing pressures such as transient water surface fluctuations. The response time of DP15 differential pressure transducers series is 0.0033 (1/300) s. The sensors were calibrated before the commencement of experiments. Two digital cameras were also used simultaneously to capture the moving pattern of rigid sliding block. One of the cameras was used for side observation and another for photographing from top view. Both of the cameras were focused on the near zone of underwater sliding.

The experimental set-up data are listed in Table 4. As it can be seen, the experiment variable parameters can be listed as follow: slide

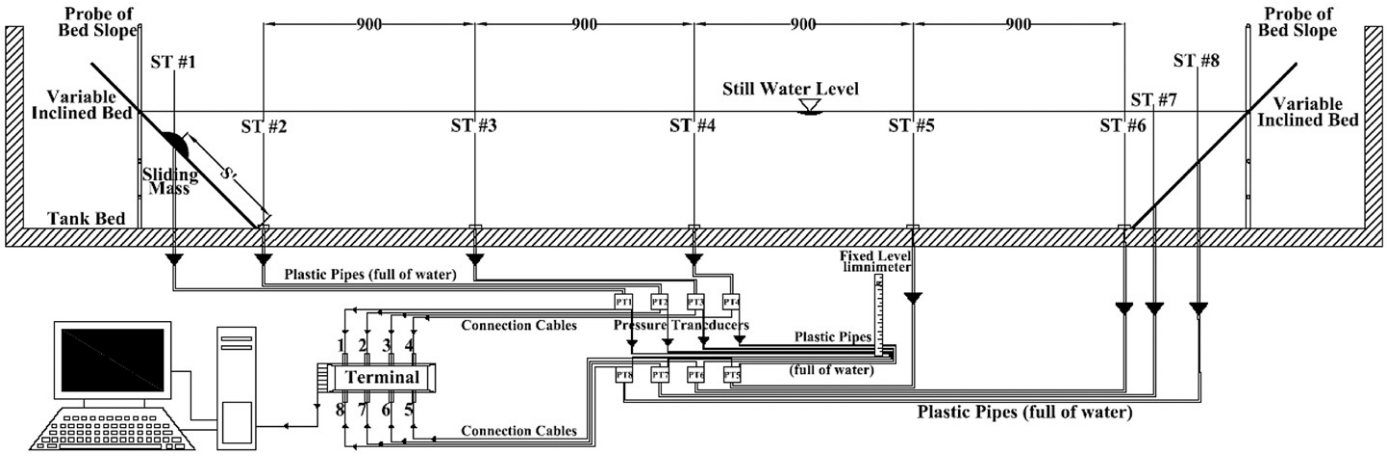

Fig. 1. Schematic of experimental set-up for underwater landslide generated waves, all dimensions are in millimeter.

Table 2
Specifications of rigid blocks

No.	Tag no.	V (m^3)	W_p (kg)	W_i (kg)	W_w (kg)	W_t (kg)	A (m^2)	γ (kg/m^3)
		±0.000001	±0.001	±0.001	±0.001	±0.001	±0.001	±0.1
1	B1	0.00390	2.37	1.14	3.90	7.41	0.0195	1900
2	B2	0.00780	3.92	3.10	7.80	14.82	0.0390*	1900
3	B3	0.00195	1.57	0.19	1.95	3.71	0.0098	1900
4	T1	0.00390	2.84	0.67	3.90	7.41	0.0195	1900
5	H5	0.00310	2.52	0.27	3.10	5.89	0.0165	1900
6	H6	0.00540	4.05	0.81	5.40	10.26	0.0165	1900
7	H7	0.00770	5.58	1.35	7.70	14.63	0.0165	1900

V: solid block volume; W_w: weight of water; W_p: weight of perimeter steel plate; W_t: total weight of sliding block; W_i: weight of additional insert plate; γ: special gravity [$=W_t/V$]; A: cross section area.
*0.0390 for B2a and 0.0600 for B2b (see Fig. 2).

Table 3
Specifications of wave gauges

No.	Gauge station	Sensor technical name	P_{max}	Ac.
1	ST1	DP-15-22-N-1-S-5A	140	±0.35
2	ST2	DP-15-32-N-1-S-5A	1400	±3.5
3	ST3	DP-15-32-N-1-S-5A	1400	±3.5
4	ST4	DP-15-32-N-1-S-5A	1400	±3.5
5	ST5	DP-15-32-N-1-S-5A	1400	±3.5
6	ST6	DP-15-22-N-1-S-5A	140	±0.35
7	ST7	DP-15-22-N-1-S-5A	140	±0.35
8	ST8	DP-15-22-N-1-S-5A	140	±0.35

P_{max}: Maximum measurable differential pressure. (Δp between two sides of diaphragm) (mm H_2O). Ac.: Accuracy (mm H_2O).

specifications such as shape, volume, thickness (T), length parallel to the bed slope (B) and rigidity (will be explained), sliding bed slope angle (θ), initial submergence of slide (h_{0C}), and still water depth in wave tank (h_0). Definition of the parameters for each of the blocks is shown in Fig. 3. The parameter S', as shown Fig. 1, is the exact location of ST1 in each test. The location of ST1 was fixed at the initial position of the mass center of submerged block before sliding. The bed slope was varied in various test sets while the initial submergence was fixed. So to capture the initial impulse wave amplitude, the location of ST1 was adjustable. The exact location of ST1 is listed in Table 4 for all of the performed tests. For adjustment of ST1, a slot of 5 mm wide and 1100 mm long was placed at the central axis of the inclined bed. The head-part of the piezometer could be moved and adjusted along the slot. The plastic pipe of the first pressure transducer connected to the head-part of piezometer in all cases. The numbering procedure of tests is illustrated in Fig. 4. All of the specifications of a case set can be observed in its test number.

Lateral dimensions of the inclined bed and the sliding blocks were much smaller than the distance between the lateral walls of wave tank. Thus the experiment conducted was three dimensional as it happens in real cases. It increases the applicability of measured data and laboratory-based estimation method for prediction of wave characteristics in real cases. To minimize the effect of wave reflection from the lateral and end boundaries of tank on the recorded data, the sponge sheets as well as punched inclined planes were installed on the lateral and end walls of tank, as it is common for laboratory wave tanks. Moreover, the lateral walls of tank were relatively far from sliding axis.

To minimize the effect of bed friction on the sliding pattern of blocks and also on the generated wave, the inclined sliding bed was completely lubricated and all of the tests were repeated, at least two times and the recorded data of slide motion was examined and reported when the recorded time-variable location of block mass center during the sliding had negligible changes.

In deforming-slide tests (cases 103 to 120 in Table 4), granular materials with a mean diameter (D_{50}) of about 7–9 mm with ρ=1.8–2.0 ton/m^3 were used. The initial shape of the granular slide was similar to the triangle section as T1 rigid block case. This similarity enables us to compare the experimental results in corresponding rigid and deformable-slide tests with the same initial geometry. The deformable-landslide tests are divided into two categories. At the first group of experiments (cases 103 to 111 in Table 4), granular materials are naturally used without any confining fabric, so after releasing of the slide, it has completely deformed and dispersed in the water body. For the second group (cases 112 to 120 in Table 4), granular materials are confined in a very soft fabric. So, the slide behaves like a dense current and the continuity of slide will be held during deformation. Fig. 5 shows some sample pictures about three conditions for slide rigidity: rigid, granular material and confined-granular material.

The data set in this experimental work covers wider ranges of parameters in comparison with the previous laboratory works. Table 5 provides a comparison for the range of the main experimental parameters in previous and present laboratory works. In this table, four main parameters which have the main role in the impulse wave characteristics in near and field are listed: sliding block shape, sliding bed slope angle, dimensionless slide thickness (maximum thickness over length parallel to the bed slope), dimensionless slide initial submergence (initial submergence over length parallel to the bed slope), and

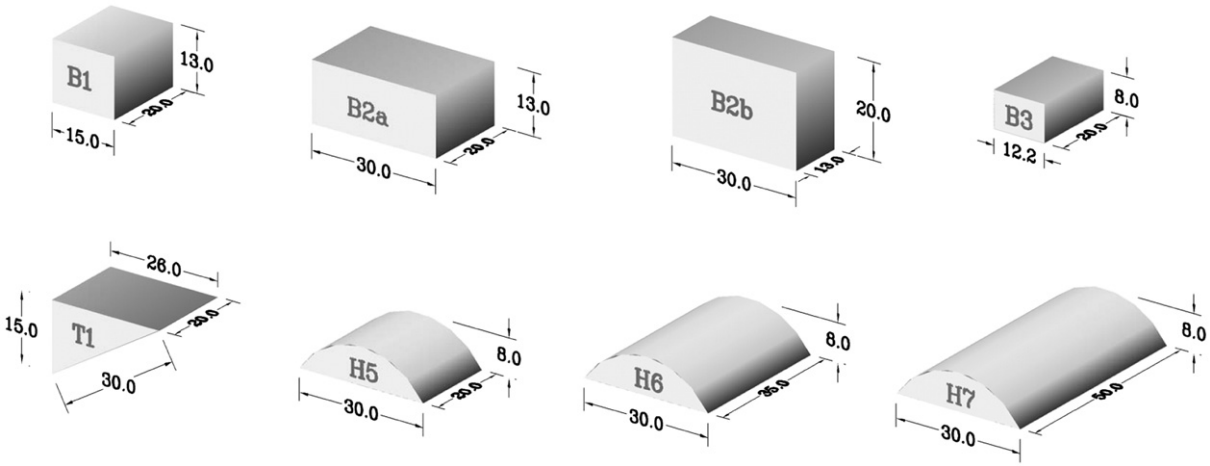

Fig. 2. Schematic of rigid blocks.

Table 4
The experimental program for 120 performed laboratory tests

Case no.	Test no.	Slide rigidity	Block tag	B (m)	T (m)	h_{0c} (m)	θ (deg)	h_0 (m)	S' (m)
1	R-B1-30-11	R	B1	0.15	0.13	0.025	30	0.8	1.3249
2	R-B1-30-21	R	B1	0.15	0.13	0.05	30	0.8	1.2749
3	R-B1-30-31	R	B1	0.15	0.13	0.1	30	0.8	1.1749
4	R-T1-30-11	R	T1	0.3	0.13	0.025	30	0.8	1.3249
5	R-T1-30-21	R	T1	0.3	0.13	0.05	30	0.8	1.2749
6	R-T1-30-31	R	T1	0.3	0.13	0.1	30	0.8	1.1749
7	R-B1-60-11	R	B1	0.15	0.13	0.025	60	0.8	0.8198
8	R-B1-60-21	R	B1	0.15	0.13	0.05	60	0.8	0.7910
9	R-B1-60-31	R	B1	0.15	0.13	0.1	60	0.8	0.7332
10	R-T1-60-11	R	T1	0.3	0.13	0.025	60	0.8	0.8198
11	R-T1-60-21	R	T1	0.3	0.13	0.05	60	0.8	0.7910
12	R-T1-60-31	R	T1	0.3	0.13	0.1	60	0.8	0.7332
13	R-T1-45-11	R	T1	0.3	0.13	0.025	45	0.8	0.9660
14	R-T1-45-21	R	T1	0.3	0.13	0.05	45	0.8	0.9307
15	R-T1-45-31	R	T1	0.3	0.13	0.1	45	0.8	0.8600
16	R-T1-45-12	R	T1	0.3	0.13	0.025	45	0.5	0.5418
17	R-T1-45-22	R	T1	0.3	0.13	0.05	45	0.5	0.5064
18	R-T1-45-32	R	T1	0.3	0.13	0.1	45	0.5	0.4357
19	R-T1-30-12	R	T1	0.3	0.13	0.025	30	0.5	0.7249
20	R-T1-30-22	R	T1	0.3	0.13	0.05	30	0.5	0.6748
21	R-T1-30-32	R	T1	0.3	0.13	0.1	30	0.5	0.5748
22	R-T1-60-12	R	T1	0.3	0.13	0.025	60	0.5	0.4734
23	R-T1-60-22	R	T1	0.3	0.13	0.05	60	0.5	0.4446
24	R-T1-60-32	R	T1	0.3	0.13	0.1	60	0.5	0.3868
25	R-B3-30-11	R	B3	0.122	0.08	0.025	30	0.8	1.4115
26	R-B3-30-21	R	B3	0.122	0.08	0.05	30	0.8	1.3615
27	R-B3-30-31	R	B3	0.122	0.08	0.1	30	0.8	1.2615
28	R-H5-30-11	R	H5	0.3	0.08	0.025	30	0.8	1.4115
29	R-H5-30-21	R	H5	0.3	0.08	0.05	30	0.8	1.3615
30	R-H5-30-31	R	H5	0.3	0.08	0.1	30	0.8	1.2615
31	R-B3-45-11	R	B3	0.122	0.08	0.025	45	0.8	1.0160
32	R-B3-45-21	R	B3	0.122	0.08	0.05	45	0.8	0.9807
33	R-B3-45-31	R	B3	0.122	0.08	0.1	45	0.8	0.9100
34	R-H5-45-11	R	H5	0.3	0.08	0.025	45	0.8	1.0160
35	R-H5-45-21	R	H5	0.3	0.08	0.05	45	0.8	0.9807
36	R-H5-45-31	R	H5	0.3	0.08	0.1	45	0.8	0.9100
37	R-B3-60-11	R	B3	0.122	0.08	0.025	60	0.8	0.8487
38	R-B3-60-21	R	B3	0.122	0.08	0.05	60	0.8	0.8198
39	R-B3-60-31	R	B3	0.122	0.08	0.1	60	0.8	0.7621
40	R-H5-60-11	R	H5	0.3	0.08	0.025	60	0.8	0.8487
41	R-H5-60-21	R	H5	0.3	0.08	0.05	60	0.8	0.8198
42	R-H5-60-31	R	H5	0.3	0.08	0.1	60	0.8	0.7621
43	R-H6-30-11	R	H6	0.3	0.08	0.025	30	0.8	1.4115
44	R-H6-30-21	R	H6	0.3	0.08	0.05	30	0.8	1.3615
45	R-H6-30-31	R	H6	0.3	0.08	0.1	30	0.8	1.2615
46	R-H7-30-11	R	H7	0.3	0.08	0.025	30	0.8	1.4115
47	R-H7-30-21	R	H7	0.3	0.08	0.05	30	0.8	1.3615
48	R-H7-30-31	R	H7	0.3	0.08	0.1	30	0.8	1.2615
49	R-H6-45-11	R	H6	0.3	0.08	0.025	45	0.8	1.0160
50	R-H6-45-21	R	H6	0.3	0.08	0.05	45	0.8	0.9807
51	R-H6-45-31	R	H6	0.3	0.08	0.1	45	0.8	0.9100
52	R-H7-45-11	R	H7	0.3	0.08	0.025	45	0.8	1.0160
53	R-H7-45-21	R	H7	0.3	0.08	0.05	45	0.8	0.9807
54	R-H7-45-31	R	H7	0.3	0.08	0.1	45	0.8	0.9100
55	R-H6-60-11	R	H6	0.3	0.08	0.025	60	0.8	0.8487
56	R-H6-60-21	R	H6	0.3	0.08	0.05	60	0.8	0.8198
57	R-H6-60-31	R	H6	0.3	0.08	0.1	60	0.8	0.7621
58	R-H7-60-11	R	H7	0.3	0.08	0.025	60	0.8	0.8487
59	R-H7-60-21	R	H7	0.3	0.08	0.05	60	0.8	0.8198
60	R-H7-60-31	R	H7	0.3	0.08	0.1	60	0.8	0.7621
61	R-B1-45-11	R	B1	0.15	0.13	0.025	45	0.8	0.9660
62	R-B1-45-21	R	B1	0.15	0.13	0.05	45	0.8	0.9307
63	R-B1-45-31	R	B1	0.15	0.13	0.1	45	0.8	0.8600
64	R-B2a-45-11	R	B2a	0.3	0.13	0.025	45	0.8	0.9660
65	R-B2a-45-21	R	B2a	0.3	0.13	0.05	45	0.8	0.9307
66	R-B2a-45-31	R	B2a	0.3	0.13	0.1	45	0.8	0.8600
67	R-B1-15-12	R	B1	0.15	0.13	0.025	15	0.5	1.3501
68	R-B1-15-22	R	B1	0.15	0.13	0.05	15	0.5	1.2535
69	R-B1-15-32	R	B1	0.15	0.13	0.1	15	0.5	1.0603
70	R-B1-45-12	R	B1	0.15	0.13	0.025	45	0.5	0.5418
71	R-B1-45-22	R	B1	0.15	0.13	0.05	45	0.5	0.5064
72	R-B1-45-32	R	B1	0.15	0.13	0.1	45	0.5	0.4357
73	R-B2a-15-12	R	B2a	0.3	0.13	0.025	15	0.5	1.3501
74	R-B2a-15-22	R	B2a	0.3	0.13	0.05	15	0.5	1.2535
75	R-B2a-15-32	R	B2a	0.3	0.13	0.1	15	0.5	1.0603
76	R-B2a-45-12	R	B2a	0.3	0.13	0.025	45	0.5	0.5418
77	R-B2a-45-22	R	B2a	0.3	0.13	0.05	45	0.5	0.5064
78	R-B2a-45-32	R	B2a	0.3	0.13	0.1	45	0.5	0.4357
79	R-B2a-30-11	R	B2a	0.3	0.13	0.025	30	0.8	1.3249
80	R-B2a-30-21	R	B2a	0.3	0.13	0.05	30	0.8	1.2749
81	R-B2a-30-31	R	B2a	0.3	0.13	0.1	30	0.8	1.1749
82	R-B2b-30-11	R	B2b	0.3	0.2	0.025	30	0.8	1.2036
83	R-B2b-30-21	R	B2b	0.3	0.2	0.05	30	0.8	1.1536
84	R-B2b-30-31	R	B2b	0.3	0.2	0.1	30	0.8	1.0536
85	R-B2a-60-11	R	B2a	0.3	0.13	0.025	60	0.8	0.8198
86	R-B2a-60-21	R	B2a	0.3	0.13	0.05	60	0.8	0.7910
87	R-B2a-60-31	R	B2a	0.3	0.13	0.1	60	0.8	0.7332
88	R-B2b-60-11	R	B2b	0.3	0.2	0.025	60	0.8	0.7794
89	R-B2b-60-21	R	B2b	0.3	0.2	0.05	60	0.8	0.7506
90	R-B2b-60-31	R	B2b	0.3	0.2	0.1	60	0.8	0.6928
91	R-B2a-30-12	R	B2a	0.3	0.13	0.025	30	0.5	0.7249
92	R-B2a-30-22	R	B2a	0.3	0.13	0.05	30	0.5	0.6748
93	R-B2a-30-32	R	B2a	0.3	0.13	0.1	30	0.5	0.5748
94	R-B2b-30-12	R	B2b	0.3	0.2	0.025	30	0.5	0.6036
95	R-B2b-30-22	R	B2b	0.3	0.2	0.05	30	0.5	0.5536
96	R-B2b-30-32	R	B2b	0.3	0.2	0.1	30	0.5	0.4536
97	R-B2a-60-12	R	B2a	0.3	0.13	0.025	60	0.5	0.4734
98	R-B2a-60-22	R	B2a	0.3	0.13	0.05	60	0.5	0.4446
99	R-B2a-60-32	R	B2a	0.3	0.13	0.1	60	0.5	0.3868
100	R-B2b-60-12	R	B2b	0.3	0.2	0.025	60	0.5	0.4330
101	R-B2b-60-22	R	B2b	0.3	0.2	0.05	60	0.5	0.4041
102	R-B2b-60-32	R	B2b	0.3	0.2	0.1	60	0.5	0.3464
103	D-T1-30-11	G.M	T1*	0.3	0.13	0.025	30	0.8	1.3249
104	D-T1-30-21	G.M	T1*	0.3	0.13	0.05	30	0.8	1.2749
105	D-T1-30-31	G.M	T1*	0.3	0.13	0.1	30	0.8	1.1749
106	D-T1-45-11	G.M	T1*	0.3	0.13	0.025	45	0.8	0.9660
107	D-T1-45-21	G.M	T1*	0.3	0.13	0.05	45	0.8	0.9307
108	D-T1-45-31	G.M	T1*	0.3	0.13	0.1	45	0.8	0.8600
109	D-T1-60-11	G.M	T1*	0.3	0.13	0.025	60	0.8	0.8198
110	D-T1-60-21	G.M	T1*	0.3	0.13	0.05	60	0.8	0.7910
111	D-T1-60-31	G.M	T1*	0.3	0.13	0.1	60	0.8	0.7332
112	Dc-T1-30-11	C.G.M	T1*	0.3	0.13	0.025	30	0.8	1.3249
113	Dc-T1-30-21	C.G.M	T1*	0.3	0.13	0.05	30	0.8	1.2749
114	Dc-T1-30-31	C.G.M	T1*	0.3	0.13	0.1	30	0.8	1.1749
115	Dc-T1-45-11	C.G.M	T1*	0.3	0.13	0.025	45	0.8	0.9660
116	Dc-T1-45-21	C.G.M	T1*	0.3	0.13	0.05	45	0.8	0.9307
117	Dc-T1-45-31	C.G.M	T1*	0.3	0.13	0.1	45	0.8	0.8600
118	Dc-T1-60-11	C.G.M	T1*	0.3	0.13	0.025	60	0.8	0.8198
119	Dc-T1-60-21	C.G.M	T1*	0.3	0.13	0.05	60	0.8	0.7910
120	Dc-T1-60-31	C.G.M	T1*	0.3	0.13	0.1	60	0.8	0.7332

R: Rigid block (no deformable slide).
G.M.: Granular material (deforming landslide).
C.G.M: Confined-granular material (confined deforming landslide).
*: initial shape of deforming slides.

block weight. It can be seen that the performed laboratory tests in this work cover a wider range in all of these main parameters.

Eight wave gauges were used in the experimental set-up. In this paper, we only use the experimental data obtained from the first six gauges (ST1 to ST6). The data analysis for recorded data at wave gauges ST7 and ST8 and analysis of the wave run-up on the end inclined bed will be reported in a consequent paper.

3. Experimental measurements

The measured data are categorized as the landslide kinematics data and the recorded water surface time series at wave gauges. At the first category, the moving pattern of underwater slides is captured with a digital camera in 25 frames per second. The location of mass center of slides is determined during sliding down at 0.04-s time step. The location is measured parallel to the bed slope and the S–t curve is determined where S is the slide mass center location. The u–t and α–t curves are found from S–t curve by two-step time derivation where u is the slide velocity and α is its acceleration. Based on u–t and α–t

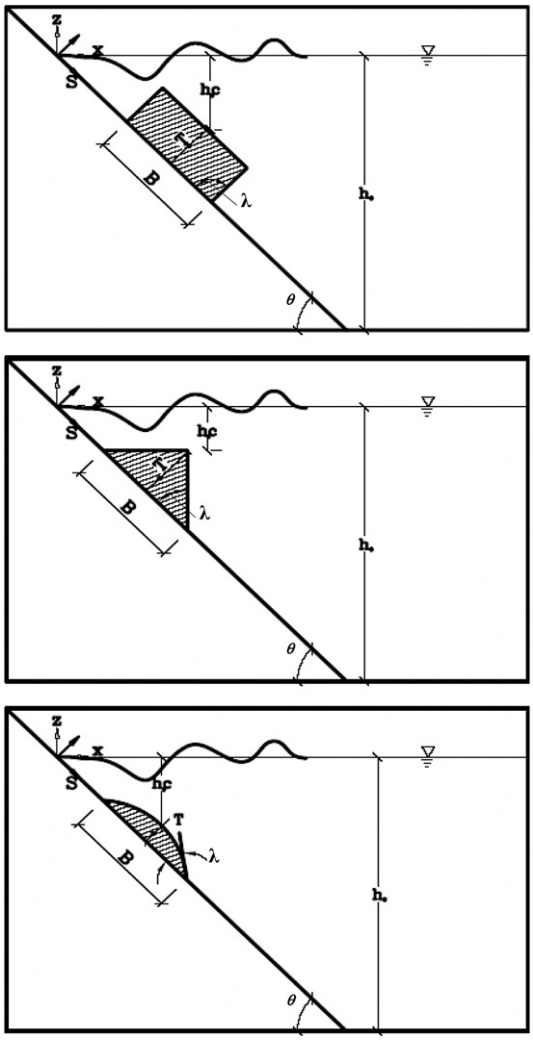

Fig. 3. Definition of geometric parameters for each of tests.

curves, the main parameters of slide kinematics, u_t (slide terminal velocity) and α_0 (slide initial acceleration) are determined. As it will be explained, the measured landslide kinematics is used to investigate the impulse wave feature and to provide forecasting methods of wave characteristics. In the second category, water surface fluctuations are recorded at wave gauges located at various distances from slide zone. The recorded time series at wave gauges are used to recognize a general feature for impulse wave in near and far-field and to investigate the impulse wave energy and nonlinearity. Full information about experimental measurements including slide kinematics data, water surface time series at the eight wave gauges and wave run-up, as well as the related pictures and movies are given on http://civil.sharif.edu/~ataie/ImpWave/SubmarinExp. As explained before, only the first six wave gauges recorded data is considered here and other two wave gauges data as well as wave run-up analysis are under preparation for a consequent paper.

4. Data analysis

4.1. Impulse wave feature

The recorded water surface time series at several wave gauges are used to recognize the general features of underwater landslide generated waves. The analysis is made separately for initial impulse wave which occurs at the sliding zone (recorded at the first wave gauge ST1) and propagating waves into the tank (recorded at wave gauges ST2 to ST6). Various experimental conditions are considered to achieve an overall view of wave feature in near and far-field.

The inspection of recorded data at the first wave gauge ST1 shows that just after moving of underwater mass, the water surface is depressed down at the point which corresponds to the slide center. The maximum depression of water surface is a basic characteristic of underwater landslide generated waves at the near-field (Watts, 1998; Lynett and Liu, 2002; Watts et al., 2005; Ataie-Ashtiani and Najafi-Jilani, 2006; Ataie-Ashtiani and Shobeyri, 2008; Ataie-Ashtiani and Najafi-Jilani, 2007). This depression is named here as the initial wave trough amplitude, a_{t1}. In front of this depression, a positive wave with a mild crest appears which propagate far from slide zone. A sample of recorded time series at ST1 is shown in Fig. 6. Zero elevation in this figure is corresponding to still water level.

As seen in Fig. 6 and based on the recorded time series at ST1, the general pattern of impulse wave at the generation zone is the same in all cases. In the cases of steeper bed, greater landslide thickness, and shallower sliding, the maximum depression of water surface increases. Laboratory data analysis shows that the maximum water surface depression (a_{t1}) is strongly affected by bed slope angle, landslide initial submergence, thickness, and kinematics and it is weakly influenced by landslide length and shape (Najafi-Jilani and Ataie-Ashtiani, 2008). Based on laboratory measurements, a general feature of near-field impulse wave can be recognized. This feature and its characteristics are shown in Fig. 7.

A similar wave pattern for impulse wave feature at generation zone has been observed in earlier laboratory works (Heinrich, 1992; Rzadkiewicz et al., 1997; Watts, 1998; Grilli et al., 2002). As shown in Fig. 7, the main characteristics of near-field wave are: initial crest amplitude; a_{c1}, corresponding time of trough amplitude; t_{at1}, corresponding time of crest amplitude; t_{ac1}, and the characteristic wave period; T_1. The results show that all of the time-scale parameters such as period are strongly related to the characteristic time of landslide motion; t_0, which is defined as $t_0 = u_t/\alpha_0$ (Watts, 1998) where u_t is the terminal velocity of underwater landslide and α_0 is its initial acceleration. These kinematics-parameters have been measured in this work. It is also concluded that the length-scale parameters such as; amplitudes and wavelength are strongly related to the maximum water depression; a_{t1} which can be recognized as significant amplitude for initial underwater landslide generated waves.

To investigate the landslide deformation effects on the impulse wave feature, the recorded data at wave gauge ST1 for cases 103 to 120 are considered and compared with corresponding data for the rigid-slide cases. Fig. 8 shows a sample of these comparisons. As seen, the impulse wave feature at the generation zone is not strongly affected by slide deformation. The general feature of waves can also be observed in deformable-slide cases. Table 6 lists wave characteristics in three

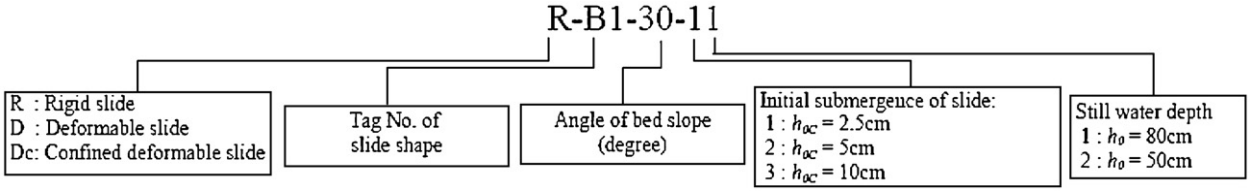

Fig. 4. Numbering procedure of laboratory tests.

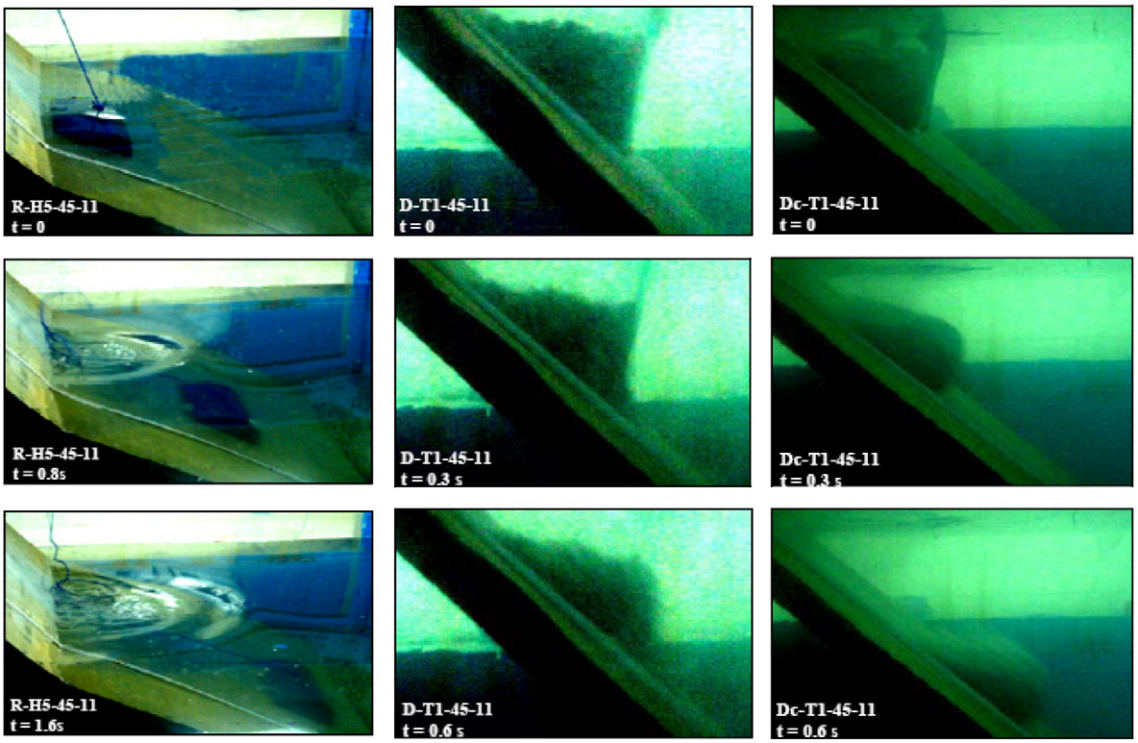

Fig. 5. Three conditions for slide rigidity from left to right: rigid, granular material and confined-granular material, (R, G.M, and C.G.M in Table 4, respectively).

conditions of the slide rigidity, including the rigid, granular deformable and confined-granular deformable cases.

The trough amplitude of initial impulse wave (a_{t1}) has a maximum reduction of 15% in deforming-slide cases. More reduction is observed in crest amplitude (a_{c1}) both in confined-granular (15 to 20%) and granular (15 to 25%) slide tests. The wave characteristic period increases about 10% in confined-granular tests and 15% in granular slides. Similar changes have been observed for corresponding time of wave trough amplitude (t_{at1}).

Effects of slide shape on the impulse wave feature are also investigated using the recorded data at ST1. Cases 1 to 12 are selected to study the influence of the shape of blocks on the wave characteristics. In these cases, two blocks B1 and T1 are used which have the same volume (=0.0039 m^3), weight (=7.41 kg), and maximum thickness perpendicular the bed slope (=0.13 m). Fig. 9 shows the time series recorded at ST1 for these cases. The main parameters such as bed slope angle and initial submergence are the same. As seen, the general feature of impulse wave is not significantly affected by the slide shape. The amplitude and period are changed less than 5%. Therefore, the effects of slide shape can be neglected comparing to the main effective parameters such as bed slope and initial submergence. From the data analysis of wave gauges ST2 to ST6, it is concluded that when the impulse wave propagated into the far-field, the wave amplitude and steepness decrease, period and wavelength increase and also the Ursell number slightly increases. The frequency dispersion of wave leads a traveling wave train with a noticeable leading wave. Fig. 10 shows a sample of the recorded data at wave gauge ST6.

Generally, the leading wave characteristics are strongly related to the water body conditions such as water depth and bed topography. For our tests over a fixed horizontal bed channel, a general feature of far-field wave can be identified in laboratory records. Fig. 11 shows the general pattern of propagated leading wave which is recognized based on measured data at wave gauges ST2 to ST6.

A leading low-amplitude positive wave can be recognized which follows by a noticeable water surface depression as a trough, again a lower-order crest, and finally a wave train with decreasing amplitude and increasing period. Similar variations were reported in previous laboratory works in which, far-field data for waves were available (Rzadkiewicz et al., 1997; Watts, 1998; Grilli et al., 2002). This is also confirmed by available numerical data which came from BIEM model (Grilli and Watts, 2005). The main specifications of leading wave feature are trough amplitude; a_t, first crest amplitude; a'_c, second crest amplitude; a_c. corresponding time of leading wave trough; t_{at}, and the characteristic leading wave period; T_p.

Table 5
Comparing the main experimental parameters in previous laboratory works and this work

Block shape		Sliding slope (deg.)		Block dimensionless thickness		Block dimensionless initial submergence		Block weight (Kg)	
Previous lab. works	Present work	Previous lab. works	Present work	Previous lab. works	Present work	Previous lab. works	Present work	Previous lab. works	Present work
Semi ellipse	Semi ellipse	15	15	0.052	0.26	0.261	0.08	0.45 1	3.7
Triangle	Triangle	45	30	0.5	0.43	0.488	0.16	14.8*	5.9
	Box		45		0.65	0.616	0.2		7.4
			60		0.86		0.33		14.8
							0.4		
							0.66		
							0.8		

* only for 15° slope.

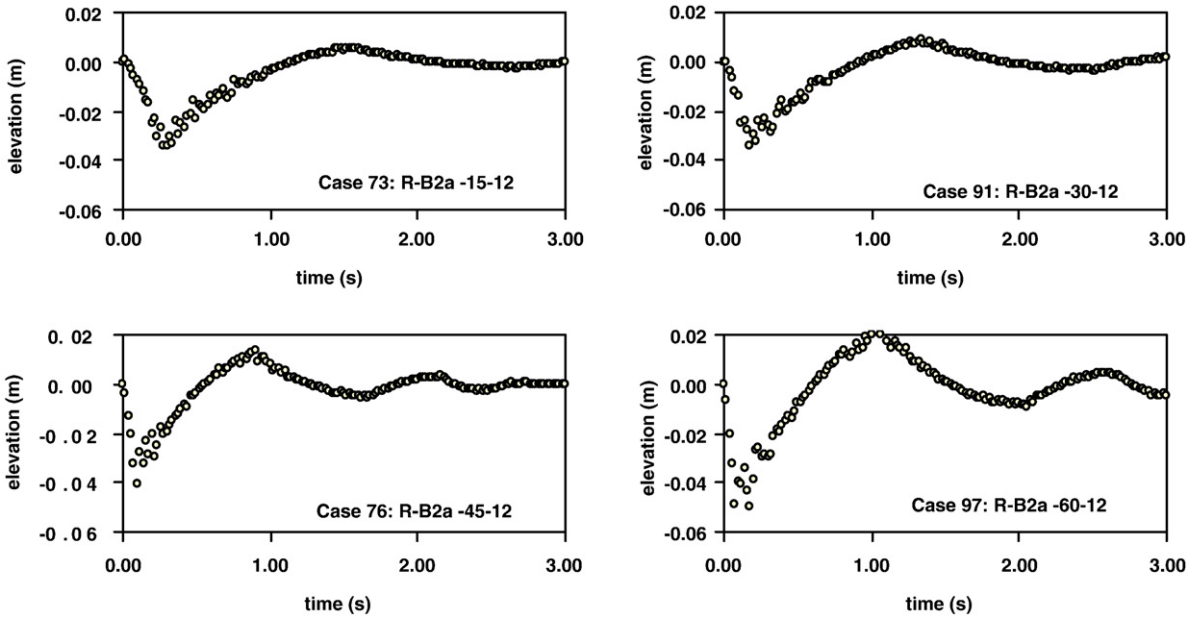

Fig. 6. Recorded time series at wave gauge ST1 for sample tests.

The measured laboratory data (Table 6) can be generally reanalyzed to categorize the parameters which affect the impulse wave characteristics and feature. The data can be used to evaluate the effective parameters and to compare the order of their effects. In this regard, it seems that all of the effective parameters may be categorized in three main groups;

1) The slide characteristics including: slide shape, deformation, dimensions and density,
2) The sliding location including: initial submergence of slide mass and sliding bed slope angle, and
3) The parameters that affect the wave during propagation in the water body including: still water depth, bottom conditions and distance of propagation.

The first categories are related to the impulse wave generation and the third one is related to its propagation. The influences of the shape of slide mass and the slide deformation can be considered as insignificant. Three different shape for landslide, including triangle, cubic and semi-ellipse, are tested and it was concluded (i.e. Fig. 9) that the effect of shape is relatively negligible on the generated impulse wave characteristics. For slide deformation, two different conditions have been tested including granular slide and cohesive slide mass and it was concluded (i.e. Fig. 8 and Table 6) that a rigid model can be used for sliding mass and this simplification does not strongly influence the impulse wave characteristics. However, the main geometrical dimensions of slide have significant influences and are an effective parameter. Wide range

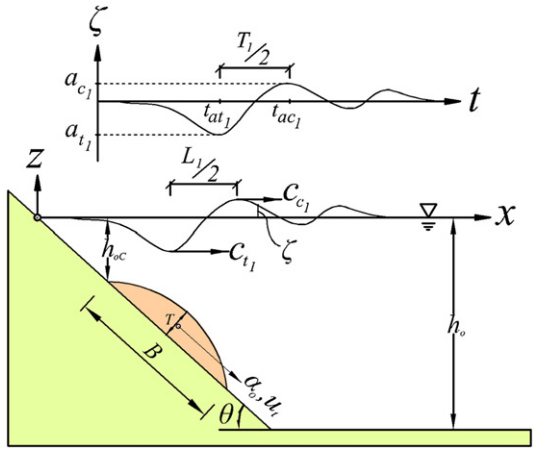

Fig. 7. General feature for near-field waves recognized at wave gauge ST1.

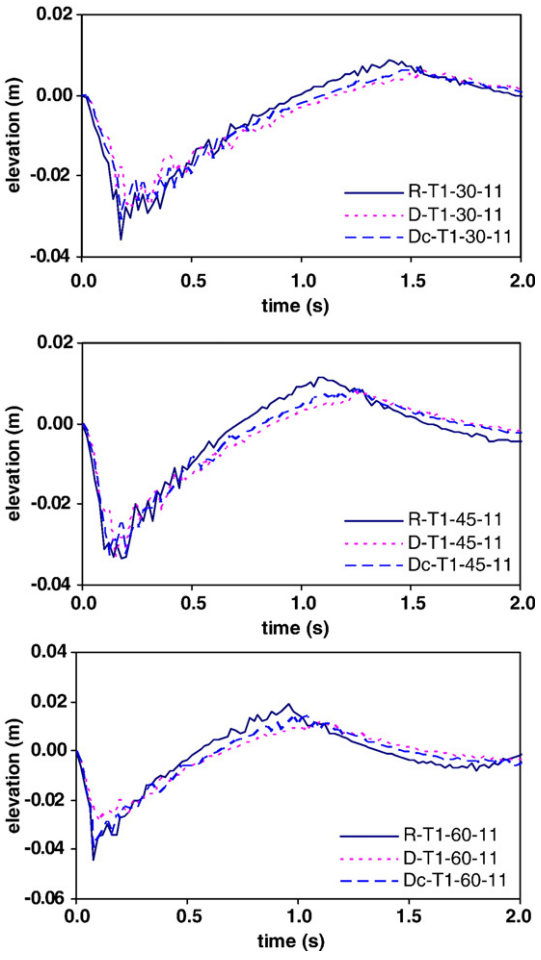

Fig. 8. Recorded time series at ST1, comparison of slide rigidity effects on impulse wave feature.

Table 6
Impulse wave characteristics recorded at wave gauge ST1, comparison of slide rigidity effects

Case no.	Test no.	at_1(m)	ac_1(m)	$t_{(at1)}$ (s)	$t_{(ac1)}$ (s)	T_1 (s)
4	R-T1-30-11	0.0313	0.0082	0.18	1.42	2.48
5	R-T1-30-21	0.0125	0.0036	0.16	1.14	1.94
6	R-T1-30-31	0.0015	0.0005	0.14	0.91	1.53
103	D-T1-30-11	0.0266	0.0068	0.20	1.84	3.28
104	D-T1-30-21	0.0104	0.0029	0.18	1.53	2.69
105	D-T1-30-31	0.0012	0.0004	0.15	1.19	2.08
112	Dc-T1-30-11	0.0282	0.0074	0.19	1.76	3.14
113	Dc-T1-30-21	0.0116	0.0034	0.16	1.45	2.58
114	Dc-T1-30-31	0.0014	0.0005	0.14	1.12	1.97
13	R-T1-45-11	0.0340	0.0140	0.11	1.33	2.44
14	R-T1-45-21	0.0150	0.0067	0.09	1.05	1.92
15	R-T1-45-31	0.0016	0.0008	0.08	0.83	1.50
106	D-T1-45-11	0.0296	0.0091	0.12	1.49	2.73
107	D-T1-45-21	0.0129	0.0042	0.11	1.21	2.20
108	D-T1-45-31	0.0013	0.0005	0.09	0.95	1.71
115	Dc-T1-45-11	0.0303	0.0101	0.11	1.43	2.64
116	Dc-T1-45-21	0.0132	0.0050	0.10	1.12	2.03
117	Dc-T1-45-31	0.0015	0.0006	0.09	0.89	1.61
10	R-T1-60-11	0.0396	0.0130	0.08	0.82	1.47
11	R-T1-60-21	0.0166	0.0059	0.07	0.65	1.15
12	R-T1-60-31	0.0035	0.0014	0.07	0.52	0.91
109	D-T1-60-11	0.0313	0.0069	0.11	0.81	1.40
110	D-T1-60-21	0.0143	0.0034	0.10	0.62	1.05
111	D-T1-60-31	0.0030	0.0007	0.08	0.50	0.83
118	Dc-T1-60-11	0.0376	0.0080	0.10	0.76	1.32
119	Dc-T1-60-21	0.0146	0.0036	0.08	0.61	1.04
120	Dc-T1-60-31	0.0031	0.0008	0.08	0.49	0.83

variations for these parameters are considered in the performed tests (Section 4.2) and it was concluded that the slide length along the bed slope, slide thickness and slide width are the main dimensions which have a main impact on the impulse wave characteristics. As a result of data analysis in the first group, five parameters can be selected as the main effective parameters, these are: B, slide length along the bed slope; T, slide maximum thickness; w, slide maximum width; γ, slide density, and lastly λ, slide front angle (Fig. 3). Although it was concluded that the slide shape can be neglected, this parameter will be considered for further investigation later on.[2]

For parameters in the second group, the selected range of variation in performed tests is wide enough (see columns 3, 4, 7, and 8 from left in Table 5) to explore their order of effects. It can be concluded that the second group includes the most important parameters which strongly affect the wave characteristics (Figs. 6 to 11 and Tables 6 and 7). The laboratory data show that when the initial submergence of slide decreases about 50%, from 10 cm to 5 cm in laboratory cases (Table 4 and 6), the impulse wave amplitude increases about 80%. The similar effect can be seen for sliding bed slope. The maximum water surface depression caused by underwater landslide or the impulse wave amplitude is strongly related to the sliding bed slope angle. Both of the parameters in the second group (i. e. h_{0C}: initial submergence of slide and θ, sliding bed slope angle) should be considered in any quantitative evaluation of impulse wave characteristics.

The third group includes the parameters which affect the impulse wave characteristics during propagation in water body. In our performed tests, the two still water depths are 50 and 80 cm. Although the test condition is relatively limited, the data can be used to study the far-field wave characteristics as the effect of wave propagation distance on the wave characteristics.

4.2. Impulse wave energy

In this section, the energy conversion of impulse wave is studied. Energy conversion analysis for underwater landslide generated waves has been studied by Watts (1998). Fritz et al. (2004) have also studied impulse wave energy for sub-aerial landslide generated waves. The impulse wave energy at the wave gauges located at various distances from the source point is calculated based on the recorded gauge data by Watts (1998) formula as:

$$E_w(x) = \rho_w g t_0 \eta(x)^2_{max} \sqrt{g h_{0C}} \quad (1)$$

where $E_w(x)$ is wave energy per unit width (kg m/s^2) at distance x from source point, ρ_w is water density (=1000 kg/m^3), g is gravity acceleration (=9.81 m/s^2), η_{max} is the maximum water surface fluctuation from still water level or the maximum trough amplitude of impulse wave in our data (a_t), and h_{0C} (m) is the initial submergence of landslide. A measure of the landslide energy is also calculated from Watts (1998) formula as:

$$E_s = \rho_s u_t^2 A \quad (2)$$

where E_s is slide energy per unit width (kg m/s^2), ρ_s is slide density (=1900 kg/m^3), u_t is slide terminal velocity (m/s), and A is cross section area of blocks (m^2). A measure for the energy conversion from the sliding block into the wave is defined as the energy conversion ratio, e_0 (Watts, 1998):

$$e_0 = \frac{E_w(0)}{E_s} \quad (3)$$

where $E_w(0)$ is impulse wave energy at generation zone (=E_w at ST1 wave gauge). The impulse wave energy, block energy, and energy conversion ratio for some of the performed tests are given in Table 7. The data in Table 7 are categorized based on the angle of sliding bed slope. Fig. 12 shows the variation of energy conversion ratio from block into the water. As seen, the sliding bed slope angle and the initial submergence of blocks have significant influences on the ratio. The energy conversion is generally increased where the initial submergence of landslide decreases. The energy conversion in mild slope is generally greater than steeper slopes. The best-fit equations are given on Fig. 12 for each of the slope angles. Considering the mentioned

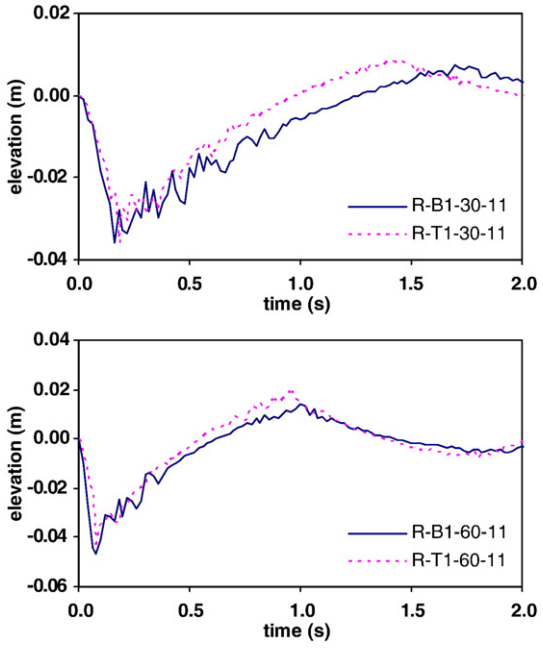

Fig. 9. Recorded time series at ST1, comparison of slide shape effects on impulse wave feature.

[2] Further quantitative analysis (Section 4.4) shows that λ is really a low-order effective parameters on wave.

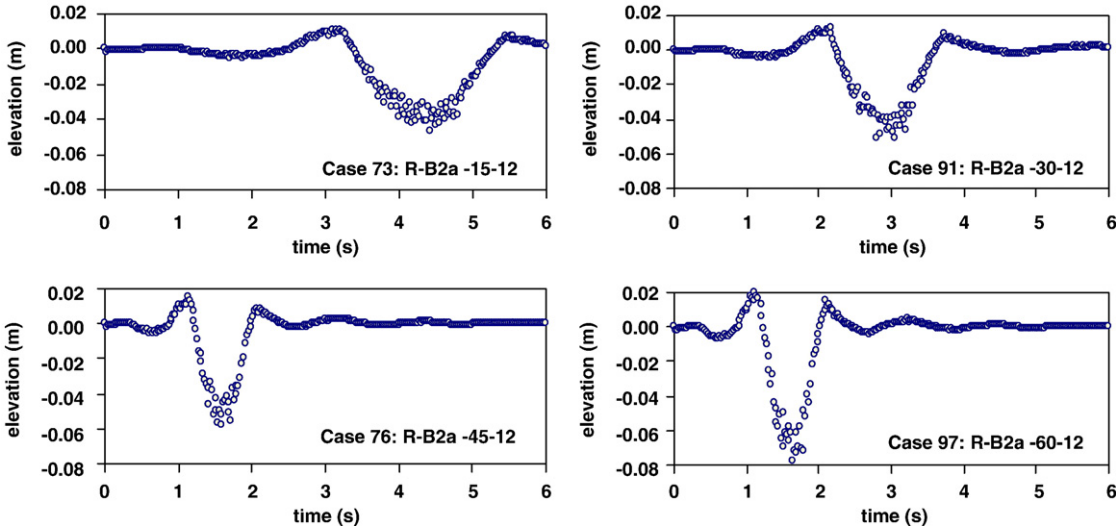

Fig. 10. Recorded time series at wave gauge ST6 for sample tests.

equations on this figure, the best-fit equation for prediction of energy conversion ratio from landslide into the water can be obtained as:

$$e_0 = \frac{E_w(0)}{E_s} = 0.0946 \cdot \left(\frac{h_{0C}}{S_0}\right)^{-2.8635} \quad (4)$$

Where h_{0C} is the initial submergence of the mass center of slide and S_0 is the characteristic length of slide kinematics and defined as $S_0 = \frac{u_t^2}{\alpha_0}$ where u_t is the terminal velocity of failure mass and α_0 is its initial acceleration. Based on the laboratory investigations of Watts (1998) the u_t and α_0 can be estimated as $u_t = \sqrt{g \cdot B} \cdot \sqrt{\frac{\pi(\gamma-1)}{2C_d}} \cdot \sin\theta$ and $\alpha_0 = g \cdot \frac{\gamma-1}{\gamma+C_m} \sin\theta$, where g is the acceleration due to gravity, B is the total length of sliding mass parallel to the bed slope, C_d and C_m are the drag and added mass coefficients, respectively, γ is the slide soil special gravity, and θ is the bed slope angle.

In our performed experiments, a range of 1 to 14% is observed for energy conversion ratio. The validity range of Eq. (4) is $\theta \in [15°, 60°]$. For further investigation on Eq. (4), the coefficient of variation is calculated for it. The coefficient of variation (CoV) is a measure of dispersion of a probability distribution. It is defined as the ratio of the standard deviation to the mean. The coefficient of variation for energy conversion ratio (e_0) in Eq. (4) is calculated as 1.12.

As seen in Fig. 12 and Eq. (4), when the initial submergence of landslide is decreased, the energy conversion from slide into wave will be strongly increased. Moreover, for steeper bed slopes the energy conversion ratio will be decreased because of the faster sliding down of failure mass. As the slide moves down faster, the contact between landslide mass and surrounding water will have a shorter contact time, the energy conversion from landslide into the water will be decreased.

As seen, the energy conversion is generally independent on the landslide shape for rigid blocks. However, the slide deformation can influence the energy conversion. As shown in Fig. 13, the slide deformation can cause an average reduction of 20% in energy conversion ratio for confined-granular material and about 30% for granular material slide in comparison of that to the rigid slide. The energy conversion ratio in granular slide is less than confined granular. In the granular slide, major part of the failure mass will be completely mixed with surrounded water and it leads to more slide energy dissipation. In the confined-granular slide, water does not penetrate into the failure mass body and it leads to less slide energy dissipation.

The wave energy propagation ratio is defined as:

$$e = \frac{E_w(x)}{E_w(0)} \quad (5)$$

that is an indication of the variation of wave energy at various distances from sliding source point in a dimensionless form. The variation of impulse wave energy during propagation into the wave tank is shown in Fig. 14. As seen, the wave energy ratio increases immediately after propagation and reaches to a maximum value as e_{max} and then, it decreases and reaches to a constant value in far-field. Similar observation was made in Watts (1998) experimental works for

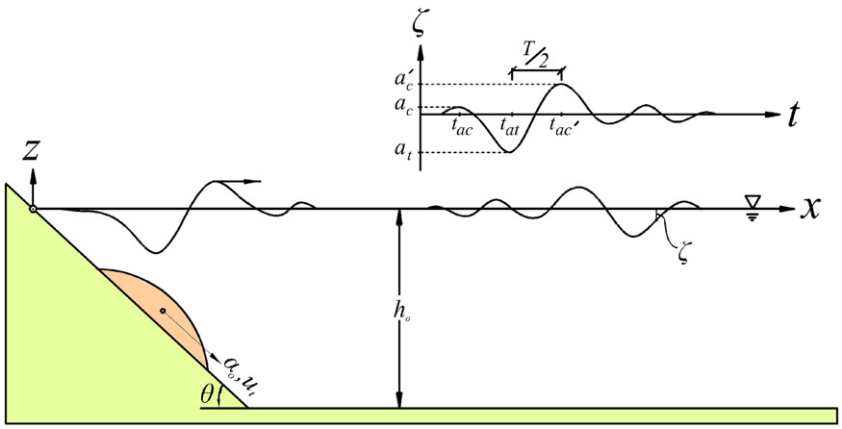

Fig. 11. General feature for far-field waves recognized based on recorded time series at wave gauge ST2 to ST6.

Table 7
Energy per unit width (kg m/s^2) for impulse wave and for landslide

Case no.	Wave energy at several wave gauges							Slide energy
	Test no.	ST1	ST2	ST3	ST4	ST5	ST6	
73	R-B2a-15-12	1.2021	2.6923	2.1825	1.9031	1.7189	1.5850	9.6034
74	R-B2a-15-22	0.0276	0.0540	0.0432	0.0375	0.0338	0.0311	9.6034
75	R-B2a-15-32	0.0169	0.0299	0.0233	0.0199	0.0179	0.0164	9.6034
3	R-B1-30-31	0.0057	0.0063	0.0049	0.0042	0.0038	0.0034	4.8017
4	R-T1-30-11	1.0111	2.8723	2.2784	1.9694	1.7703	1.6275	9.2625
5	R-T1-30-21	0.2281	0.5571	0.4389	0.3784	0.3396	0.3120	9.2625
6	R-T1-30-31	0.0046	0.0099	0.0077	0.0066	0.0059	0.0054	9.2625
19	R-T1-30-12	1.0111	3.0294	2.1225	1.7635	1.5546	1.4126	9.2625
20	R-T1-30-22	0.2281	0.5953	0.4101	0.3392	0.2985	0.2709	9.2625
21	R-T1-30-32	0.0046	0.0109	0.0072	0.0059	0.0052	0.0047	9.2625
28	R-H5-30-11	0.3472	1.2913	1.0356	0.8990	0.8100	0.7458	6.6337
29	R-H5-30-21	0.0765	0.2444	0.1948	0.1687	0.1518	0.1397	6.6337
30	R-H5-30-31	0.0062	0.0174	0.0137	0.0118	0.0106	0.0097	6.6337
43	R-H6-30-11	0.9592	3.0162	2.4189	2.0999	1.8920	1.7420	7.8375
44	R-H6-30-21	0.0841	0.2272	0.1811	0.1568	0.1411	0.1298	7.8375
45	R-H6-30-31	0.0141	0.0332	0.0261	0.0225	0.0202	0.0185	7.8375
46	R-H7-30-11	1.3491	3.8117	3.0568	2.6538	2.3910	2.2014	11.2860
47	R-H7-30-21	0.1240	0.3009	0.2398	0.2077	0.1869	0.1719	11.2860
48	R-H7-30-31	0.0242	0.0513	0.0404	0.0348	0.0312	0.0287	11.2860
79	R-B2a-30-11	0.9947	3.1585	2.5054	2.1656	1.9467	1.7897	20.8147
80	R-B2a-30-21	0.0798	0.2180	0.1718	0.1481	0.1329	0.1221	20.8147
81	R-B2a-30-31	0.0153	0.0366	0.0284	0.0244	0.0218	0.0200	20.8147
82	R-B2b-30-11	0.7692	2.4310	1.8952	1.6275	1.4579	1.3375	29.6514
83	R-B2b-30-21	0.0731	0.1988	0.1538	0.1317	0.1178	0.1080	29.6514
84	R-B2b-30-31	0.0156	0.0372	0.0283	0.0241	0.0215	0.0196	29.6514
91	R-B2a-30-12	0.9947	2.9846	2.0911	1.7375	1.5316	1.3917	20.8147
92	R-B2a-30-22	0.0798	0.2087	0.1438	0.1189	0.1046	0.0950	20.8147
93	R-B2a-30-32	0.0153	0.0362	0.0239	0.0196	0.0172	0.0156	20.8147
94	R-B2b-30-12	0.7692	2.3786	1.5936	1.3099	1.1491	1.0413	29.6514
95	R-B2b-30-22	0.0731	0.1980	0.1298	0.1061	0.0929	0.0841	29.6514
96	R-B2b-30-32	0.0156	0.0387	0.0240	0.0195	0.0170	0.0153	29.6514
103	D-T1-30-11	0.7305	2.3162	1.8373	1.5881	1.4276	1.3124	9.2625
104	D-T1-30-21	0.1571	0.4283	0.3375	0.2909	0.2611	0.2399	9.2625
105	D-T1-30-31	0.0030	0.0073	0.0056	0.0048	0.0043	0.0040	9.2625
112	Dc-T1-30-11	0.8190	2.5967	2.0598	1.7805	1.6005	1.4714	9.2625
113	Dc-T1-30-21	0.1972	0.5378	0.4237	0.3652	0.3279	0.3012	9.2625
114	Dc-T1-30-31	0.0042	0.0100	0.0078	0.0067	0.0060	0.0055	9.2625
13	R-T1-45-11	0.8116	3.5148	2.5113	2.0975	1.8534	1.6865	11.2076
14	R-T1-45-21	0.2234	0.8315	0.5890	0.4908	0.4333	0.3940	11.2076
15	R-T1-45-31	0.0036	0.0117	0.0081	0.0067	0.0059	0.0054	11.2076
16	R-T1-45-12	0.8116	2.9627	1.8269	1.4770	1.2865	1.1612	11.2076
18	R-T1-45-32	0.0036	0.0103	0.0059	0.0048	0.0041	0.0037	11.2076
34	R-H5-45-11	0.3356	1.7231	1.2452	1.0433	0.9233	0.8409	9.8314
35	R-H5-45-21	0.1362	0.6006	0.4306	0.3600	0.3182	0.2897	9.8314
36	R-H5-45-31	0.0066	0.0254	0.0179	0.0149	0.0131	0.0120	9.8314
49	R-H6-45-11	0.8052	3.4951	2.5257	2.1163	1.8728	1.7057	12.0509
50	R-H6-45-21	0.0695	0.2592	0.1858	0.1553	0.1373	0.1250	12.0509
51	R-H6-45-31	0.0131	0.0425	0.0300	0.0249	0.0220	0.0200	12.0509
52	R-H7-45-11	0.7767	3.0292	2.1890	1.8342	1.6232	1.4783	14.9257
53	R-H7-45-21	0.0698	0.2339	0.1677	0.1402	0.1239	0.1128	14.9257
54	R-H7-45-31	0.0144	0.0421	0.0297	0.0247	0.0218	0.0198	14.9257
63	R-B1-45-31	0.0138	0.0211	0.0147	0.0122	0.0107	0.0097	6.8505
64	R-B2a-45-11	0.7196	2.8114	2.0087	1.6777	1.4825	1.3490	27.5726
65	R-B2a-45-21	0.0332	0.1114	0.0789	0.0658	0.0581	0.0528	27.5726
66	R-B2a-45-31	0.0121	0.0355	0.0247	0.0205	0.0180	0.0164	27.5726
70	R-B1-45-12	0.8333	1.5879	0.9791	0.7916	0.6895	0.6224	6.8505
76	R-B2a-45-12	0.7613	2.7829	1.7160	1.3874	1.2084	1.0908	27.5726
77	R-B2a-45-22	0.0351	0.1117	0.0675	0.0544	0.0473	0.0427	27.5726
78	R-B2a-45-32	0.0128	0.0366	0.0212	0.0169	0.0147	0.0132	27.5726
106	D-T1-45-11	0.6143	2.6603	1.9008	1.5876	1.4028	1.2765	11.2076
107	D-T1-45-21	0.1652	0.6150	0.4357	0.3630	0.3204	0.2914	11.2076
108	D-T1-45-31	0.0025	0.0083	0.0057	0.0048	0.0042	0.0038	11.2076
115	Dc-T1-45-11	0.6429	2.7841	1.9892	1.6614	1.4681	1.3359	11.2076
116	Dc-T1-45-21	0.1730	0.6439	0.4562	0.3801	0.3355	0.3051	11.2076
117	Dc-T1-45-31	0.0030	0.0099	0.0069	0.0057	0.0050	0.0046	11.2076
9	R-B1-60-31	0.0030	0.0057	0.0035	0.0028	0.0024	0.0022	10.4073
10	R-T1-60-11	0.8000	3.8076	2.3924	1.9408	1.6929	1.5293	13.7863
11	R-T1-60-21	0.1988	0.8128	0.5057	0.4095	0.3569	0.3223	13.7863
12	R-T1-60-31	0.0125	0.0446	0.0272	0.0219	0.0191	0.0172	13.7863
22	R-T1-60-12	0.8000	3.5211	1.8798	1.4887	1.2860	1.1556	13.7863
23	R-T1-60-22	0.1988	0.7598	0.3976	0.3141	0.2711	0.2435	13.7863
24	R-T1-60-32	0.0125	0.0428	0.0214	0.0168	0.0145	0.0130	13.7863
40	R-H5-60-11	1.1794	6.0005	3.8061	3.0932	2.7001	2.4401	12.4428
42	R-H5-60-31	0.0197	0.0750	0.0462	0.0373	0.0325	0.0293	12.4428
55	R-H6-60-11	1.3230	5.6907	3.6096	2.9335	2.5607	2.3141	14.0730
56	R-H6-60-21	0.1126	0.4158	0.2613	0.2120	0.1849	0.1670	14.0730
57	R-H6-60-31	0.0243	0.0782	0.0481	0.0389	0.0339	0.0306	14.0730
58	R-H7-60-11	1.4800	5.7201	3.6283	2.9486	2.5739	2.3261	16.2518
59	R-H7-60-21	0.1274	0.4228	0.2656	0.2155	0.1880	0.1698	16.2518
60	R-H7-60-31	0.0273	0.0790	0.0487	0.0393	0.0343	0.0309	16.2518
109	D-T1-60-11	0.4993	2.1291	1.3378	1.0853	0.9466	0.8551	13.7863
110	D-T1-60-21	0.1470	0.5386	0.3351	0.2713	0.2365	0.2135	13.7863
111	D-T1-60-31	0.0090	0.0289	0.0176	0.0142	0.0123	0.0111	13.7863
118	Dc-T1-60-11	0.7220	3.0788	1.9345	1.5694	1.3689	1.2366	13.7863
119	Dc-T1-60-21	0.1540	0.5639	0.3508	0.2841	0.2476	0.2236	13.7863
120	Dc-T1-60-31	0.0099	0.0317	0.0193	0.0156	0.0135	0.0122	13.7863

45° bed slope. Using regression method, the value of e_{max} and its corresponding distance from source point is determined as:

$$e_{max} = (3.03\sin\theta - 0.27)\cdot\left(\frac{h_{0C}}{B}\right)^{(0.7\sin\theta - 3.17)} \quad (6)$$

that occurs at a distance from source point as $x|_{e=e_{max}} = 0.7h_0(\sin\theta)^{-1.17}$ where h_0 is still water depth in the wave tank. Fig. 15 shows the effects of the slide deformation on wave energy propagation ratio. As shown in Fig. 15, the slide deformations do not have significant effects on the wave energy propagation ratio. The general pattern of energy propagation ratio is similar, in performed experiments, for rigid blocks and deformable slides. The values of e_{max} and corresponding distance are also the same for rigid and deformable tests.

The maximum wave energy ratio during propagation ($E_w(x)/E_w(0)$) decreases due to slide deformation. The depression is about 20% for confined granular and about 30% for granular sliding material. This is similar to the slide deformation effects on energy conversion from slide to wave which was discussed. It can be concluded that the slide deformation mainly affect the wave generation zone. In the wave propagation stage, the initial effects of slide deformation (which was in the generation zone) are preserved.

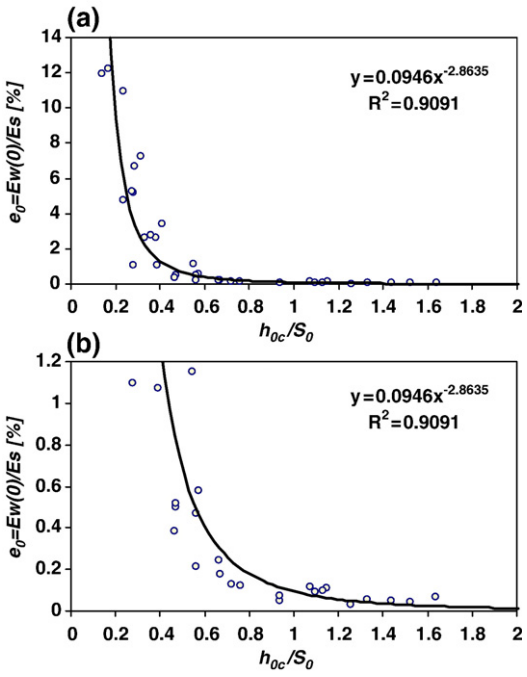

Fig. 12. Landslide energy conversion into wave energy in various slope angle and initial submergence of slide, $E_w(0)$ is wave energy at wave gauge ST1, E_b is block kinetic energy, h_{0C} is initial submergence of block and B is block length parallel to the bed slope.

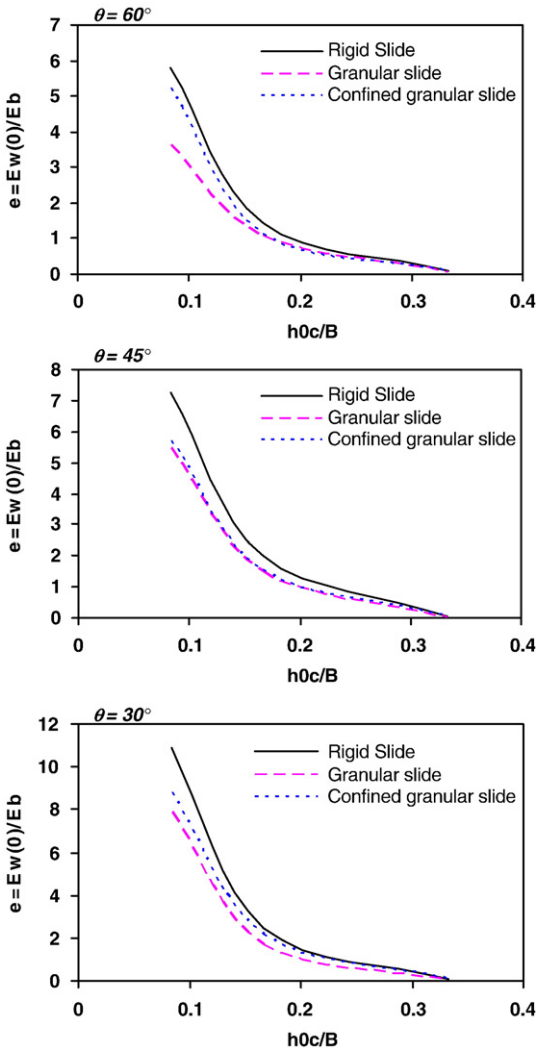

Fig. 13. Effects of landslide deformation on energy conversion from landslide into impulse wave, block energy for deformable slide is assumed equal to corresponding rigid block with the same initial shape and weight.

4.3. Impulse wave nonlinearity

Recorded data at wave Gauge ST1 is used to study the impulse wave nonlinearity at the generation zone and to examine the effect of the slide specifications on the wave nonlinearity. Three main criterions for wave nonlinearity are used here. First, the relative wave amplitude which is the wave amplitude to water depth ratio (a/h). The wave recognized as a linear wave when this ratio is less than 0.03 (Dean and Dalrymple, 1991). Second, the well-validated Ursell number which is generally defined as $U=aL^2/h^3$ where a is the wave amplitude, L is the wavelength and h is the still water depth. For linear waves this number is less than one (Lighthill, 1978). Third, wave steepness which is defined as a/L and for linear waves it is less than 0.003 (Dean and Dalrymple, 1991). These criterions were used by Fritz et al. (2004) to investigate the impulse wave nonlinearity due to sub-aerial landslide. Here, the analysis is focused on submarine slide and its relevant effective parameters such as initial submergence. The effect of various parameters on the initial wave nonlinearity is analyzed. A sample results is shown in Fig. 16 in which, the wave steepness criteria is considered.

Based on the analysis results, impulse wave is generally nonlinear except for small amplitude waves, observed in deeper sliding (in cases of $h_{0C}=10$ cm) or in very mild bed slopes. It can be also concluded that the order or effectiveness of parameters on the impulse wave nonlinearity is as follow: initial submergence of slide, sliding bed slope angle, slide thickness and lastly still water depth.

4.4. Forecasting of impulse wave characteristics

The recorded data at wave gauges are analyzed to present prediction equations for impulse wave characteristics. The main characteristics of impulse wave which are considered here are; trough amplitude, crest amplitude, period, and corresponding time of wave amplitudes. The prediction equations are separately presented for near and far-field. To define possible general forms of regressive formulations, the main dimensionless variables which govern the wave feature shall be defined. Based on laboratory observations, the

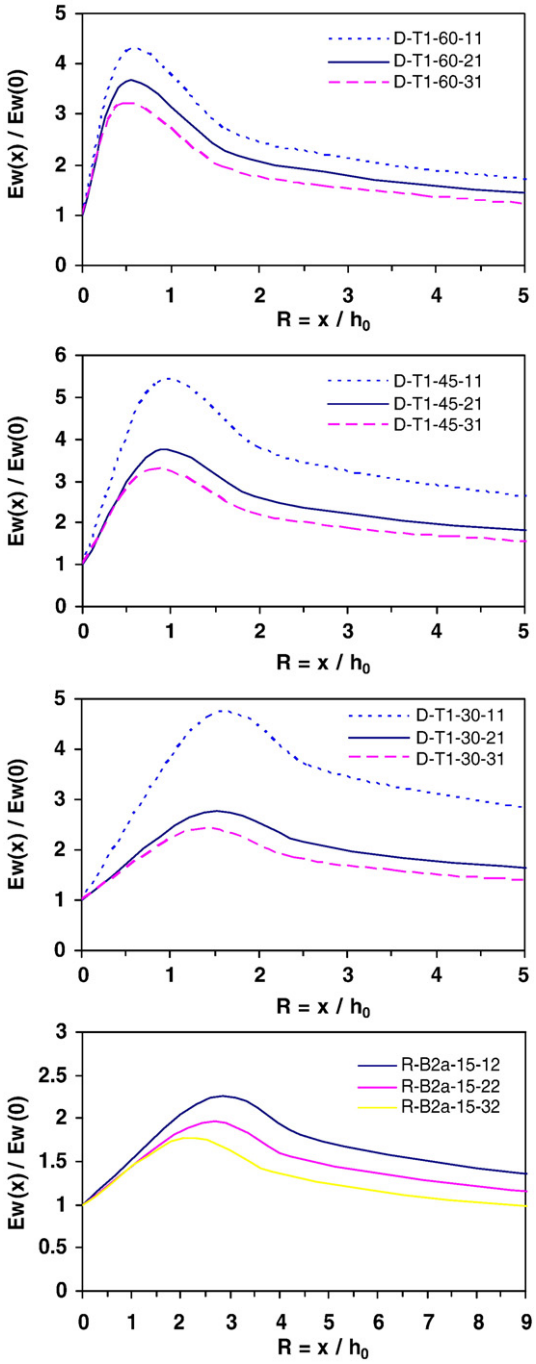

Fig. 14. Variation of wave energy during propagation, $E_w(x)$ is wave energy at distance x from source point (slide initial center), $E_w(0)$ is wave energy at the source, h_0 is still water depth in wave tank.

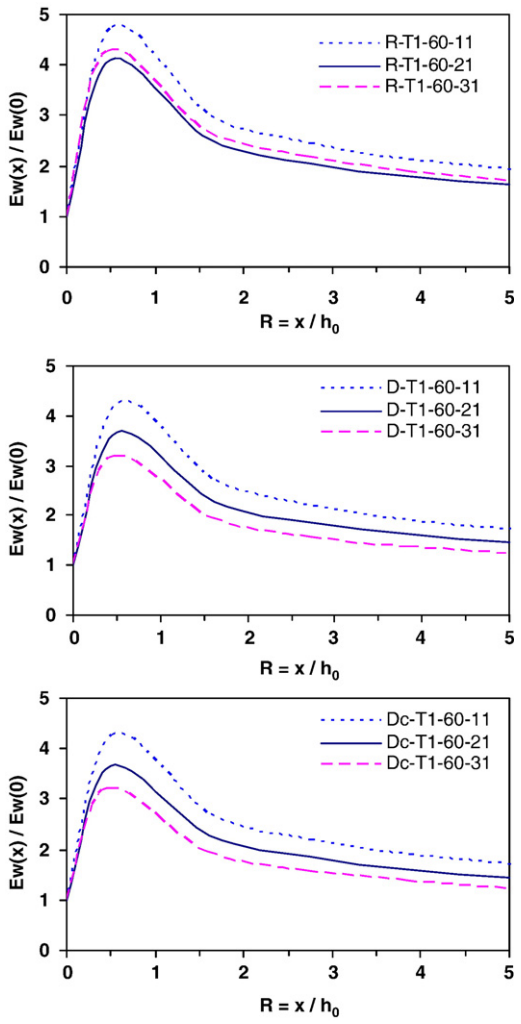

Fig. 15. Effects of landslide deformation on wave energy during propagation into the wave tank, R: rigid, D: deformable and Dc: confined deformable slide.

parameters which play main role in impulse wave feature can be categorized as follows: 1) landslide characteristics, and 2) water body conditions. First category includes slide geometry, kinematics, specific gravity (ρ_s), initial submergence (h_{0C}), and bed slope angle (θ). The slide geometry can be properly defined with slide length parallel to the bed slope (B), and its maximum thickness (T) (Enet et al., 2003). Slide kinematics can be defined with initial acceleration (α_0) and terminal velocity (u_t) and the main characteristic of slide kinematics can be expressed as $S_0=u_t^2/\alpha_0$ (Watts, 1998). Second category includes water density (ρ_w), still water depth (h_0), acceleration due to gravity (g), and the wave propagation distance (x_p).

Seven main dimensionless parameters of landslide generated waves are introduced as follow (Lynett and Liu, 2004):

$\varepsilon=T/h_{0C}$	dimensionless slide thickness
$\mu=2\pi T/B$	a measure of the steepness of the slide, named slide number
$A=B/w$	aspect ratio of the slide where w is slide width
$\gamma=\rho_s/\rho_w$	as slide density
$S=\tan\theta$	as sliding bed slope, and
$\kappa=\sin\lambda$	a measure of the slide shape where λ is the front face angle of slide (Fig. 3).
$R=x_p/h_0$	dimensionless distance of wave propagation,

Based on tests specifications listed in Table 4, variation ranges of dimensionless groups are; dimensionless slide thickness: $0.8\le\varepsilon\le8$, slide number: $1.7\le\mu\le5.5$, slide aspect ratio: $0.6\le A\le2.3$, slide density: $1.7\le\gamma\le1.9$, sliding bed slope: $0.3\le S\le1.7$, and slide shape factor: $0\le\kappa\le1$. These dimensionless parameters are used in general form of forecasting equations for prediction of wave characteristics. The prediction equations are provided for four main characteristics of impulse wave at generation zone: a_{c1}, T_1, t_{at1} and t_{ac1}:

$$a_{c1}=0.92a_{t1}\varepsilon^{-0.12}\mu^{-0.15}A^{0.23}\gamma^{-1.2}S^{0.41}\kappa^{0.005} \quad (7)$$

$$t_{at1}=3.5t_0\varepsilon^{0.18}\mu^{-0.35}A^{0.14}\gamma^{-2.3}S^{-0.15}\kappa^{0.015} \quad (8)$$

$$T_1=3.4t_0\varepsilon^{0.35}\mu^{0.17}A^{0.12}\gamma^{0.97}S^{0.34}\kappa^{0.005} \quad (9)$$

$$t_{ac1}=t_{at1}+0.5T_1 \quad (10)$$

Fig. 7 can be used as a definition sketch of impulse wave characteristics in generation zone. All of four predicted parameters in above equations are clearly illustrated in Fig. 7. The coefficient of variation of four predicted parameters in Eqs. (7)–(10) is calculated as 1.14, 0.98, 0.98, and 0.98, respectively. An applied approach for prediction of a_{t1} which is used in above equations has been presented and verified by Najafi-Jilani and Ataie-Ashtiani (2008).The forecasting equations are also provided for five main characteristics of impulse wave in far-field: a_t, a_c', a_c, t_{at}, and T_p:

$$a_t=1.3a_{t1}\varepsilon^{0.12}\mu^{-0.32}A^{0.15}\gamma^{0.7}S^{0.1}\kappa^{0.005}R^{-0.2} \quad (11)$$

$$a_{c'}=0.4a_t\varepsilon^{0.15}\mu^{-0.33}A^{0.11}\gamma^{0.55}S^{0.22}\kappa^{0.003}R^{0.4} \quad (12)$$

$$a_c=0.3a_t \quad (13)$$

$$t_{at}=0.35T_1\varepsilon^{0.1}\mu^{-0.5}A^{0.11}\gamma^{1.3}S^{0.22}\kappa^{0.002}R^{0.44} \quad (14)$$

$$T_p=0.22T_1\varepsilon^{0.12}\mu^{-0.55}A^{0.11}\gamma^{0.41}S^{-0.91}\kappa^{0.005}R^{0.12} \quad (15)$$

Fig. 11 can be used as a definition sketch of impulse wave characteristics in propagation stage. All of five predicted parameters in above equations are clearly illustrated in Fig. 11. The coefficient of variation of four predicted parameters in Eqs. (11)–(15) is calculated as 1.12, 1.07, 1.07, 0.99, and 0.98, respectively.

Based on the previous investigations (Ataie-Ashtiani and Najafi-Jilani, 2006; Najafi-Jilani and Ataie-Ashtiani, 2008), the following

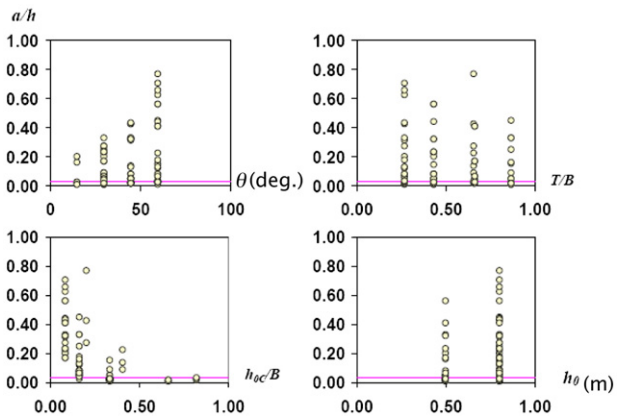

Fig. 16. Effect of slope angle (θ), thickness (T), initial submergence (h_{0c}) and still water depth (h_0) on wave steepness, the nonlinearity limit ($a/h=0.03$) is shown on the figures.

Table 8
Specifications of previous works used for verification of presented forecasting equations, (*L* for laboratory and *N* for numerical)

No.	References	Status		Test specifications										
		L	*N*	h_0 (m)	*B* (m)	*T* (m)	C_m (–)	C_d (–)	γ (–)	θ (deg)	h_{0C} (m)	u_t (m/s)	α_0 (m/s^2)	t_0 (s)
1	Heinrich (1992)	♠		1	0.707	0.353	1	1	2	45	0.01	2.775	2.782	0.997
2	Rzadkiewicz et al. (1997)	♠		1.6	0.919	0.796	1	1	1.95	45	0.1	3.084	2.688	1.147
3	Watts (1998)—2*o*	♠		0.4	0.121	0.0608	0.85	1.6	1.225	45	0.0745	0.37	0.83	0.445
4	Watts (1998)—2*a*	♠		0.4	0.121	0.0608	0.79	1.73	1.46	45	0.0745	0.44	1.2	0.366
5	Watts (1998)—2*b*	♠		0.4	0.121	0.0608	0.88	1.6	1.71	45	0.0745	0.54	1.45	0.37
6	Watts (1998)—2*n*	♠		0.4	0.121	0.0608	0.75	1.75	1.87	45	0.059	0.56	1.63	0.343
7	Watts (1998)—2*d*	♠		0.4	0.121	0.0608	0.81	1.67	2.18	45	0.0745	0.65	1.95	0.333
8	Watts (1998)—2*e*	♠		0.4	0.121	0.0608	0.68	1.62	2.465	45	0.0745	0.710	2.220	0.320
9	Watts (1998)—2*l*	♠		0.4	0.121	0.0608	0.77	1.57	2.745	45	0.0745	0.800	2.410	0.332
10	Grilli et al. (2002)	♠		1.05	1	0.052	1.76	1.53	1.81	15	0.261	1.453	1.447	1.004
11	Grilli and Watts (2005)		♠	2	1	0.052	1	1	1.85	15	0.625	1.841	1.903	0.968
12	Grilli and Watts (2005)		♠	2	1	0.052	1	1	1.85	15	0.259	1.841	1.903	0.968
13	Grilli and Watts (2005)		♠	2	1	0.052	1	1	1.85	15	0.175	1.841	1.903	0.968
14	Grilli and Watts (2005)		♠	2	1	0.052	1	1	1.85	15	0.125	1.841	1.903	0.968

equation can be used for the prediction of impulse wave amplitude in near-field (a_{t1}) is presented as:

$$a_0 = S_0 \cdot f_1(T/B,\theta) \cdot \left(\frac{h_{0C}}{B}\right)^{f_2(T/B,\theta)} \tag{16}$$

where

$$f_1(T/B,\theta) = a_1\left(\frac{T}{B}\right)^2 + a_2\left(\frac{T}{B}\right) + a_3 \tag{17}$$

$$f_2(T/B,\theta) = b_1 L_n\left(\frac{T}{B}\right) + b_2 \tag{18}$$

and the coefficients a_1, a_2, a_3, b_1, and b_2, are defined as:

$$\begin{bmatrix} a_1 \\ a_2 \\ a_3 \\ b_1 \\ b_2 \end{bmatrix} = \begin{bmatrix} 1.44976 & -2.02732 & 0.71456 & -0.04967 \\ -0.00692 & 0.14119 & -0.04103 & 0.00308 \\ 0.00580 & -0.00913 & 0.00309 & 0.00019 \\ 9.68278 & -12.68411 & 4.64830 & -0.65307 \\ 19.23503 & -27.66358 & 12.49724 & -3.72730 \end{bmatrix} \times \begin{bmatrix} \sin^3\theta \\ \sin^2\theta \\ \sin\theta \\ 1 \end{bmatrix} \tag{19}$$

Ataie-Ashtiani and Najafi-Jilani (2006) showed that when $\gamma \neq \gamma_{ref}$, the predicted wave amplitude from Eq. (16) shall be multiplied by a correction factor as $c_\gamma = c_1 + c_2\gamma$ where $c_1 = -9.21\sin^3\theta + 9.07\ \sin^2\theta - 1.82\sin\theta + 0.302$ and $c_2 = 3.26\sin^3\theta - 2.13\ \sin^2\theta - 0.15\sin\theta + 0.36$. The reference value of sliding mass density is assumed as $\gamma_{ref} = 1.9 \pm 0.05$. Moreover, the characteristic time of slide kinematics (i. e. t_0) can be calculated as $t_0 = u_t/\alpha_0$ where u_t (slide terminal velocity) and α_0 (its initial acceleration) and can be estimated as $u_t = \sqrt{g \cdot B} \cdot \sqrt{\frac{\pi(\gamma-1)}{2C_d}} \cdot \sin\theta$ and $\alpha_0 = g \cdot \frac{\gamma-1}{\gamma+C_m}\sin\theta$ (Watts, 1998). Both parameters a_{t1} and t_0 are used as scaling parameters in forecasting equations of impulse wave characteristics.

The forecasting equations have been verified using available numerical and laboratory data in previous published works. The prediction equations are verified for both near and far-field characteristics of impulse wave. The measured data presented by Heinrich (1992), Rzadkiewicz et al. (1997), Watts (1998), and Grilli et al. (2002) have been used to examine the prediction equations. Moreover, the numerical results of Grilli and Watts (2005) have also been used. Table 8 shows the detail specifications of the previous laboratory or numerical experiments. The measured and predicted impulse wave characteristics in near-field and far-field are given in Tables 9 and 10, respectively. The comparison of predicted wave characteristics and measured data in near-field are shown in Fig. 17. Similar comparison for far-field characteristics of leading impulse wave are shown in Fig. 18. The accuracy of prediction equations for length-scale parameters is generally higher than time-scales. In general, an acceptable reliability has been obtained for the presented forecasting equations.

The parameters that have been presented in Tables 9 and 10 and also illustrated in Figs. 17 and 18 include a wide range of effective values. The comparison in these figures and tables are made between the predicted wave characteristics using present formula in this work and the measured wave characteristics in previous works. The comparison includes 11 laboratory and 4 numerical cases in previous works. The available data in literature is used in this comparison to

Table 9
Verification of presented forecasting equations, near-field characteristics

No.	References	Data status		Near-field impulse wave characteristics									
				a_{t1} (mm)		a_{c1} (mm)		t_{at1} (s)		t_{ac1} (s)		T_1 (s)	
		Lab	*Num*	Measured	Predicted	Measured	Predicted	Measured	Predicted	Measured	Predicted	Measured	Predicted
1	Heinrich (1992)	♠		220	240	60	58.8	0.9	1.01	15.9	16.5	30	31.08
2	Rzadkiewicz et al. (1997)	♠		60	60	20	19.3	0.8	0.80	12.3	12.5	23	23.5
3	Watts (1998)—2*o*	♠		2.5	2.5	1.6	1.62	0.6	0.64	1.7	1.71	2.2	2.13
4	Watts (1998)—2*a*	♠		3.0	2.7	1.5	1.58	0.33	0.35	1.38	1.39	2.1	2.08
5	Watts (1998)—2*b*	♠		3.7	3.7	1.5	1.61	0.27	0.25	1.37	1.48	2.2	2.46
6	Watts (1998)—2*n*	♠		5.5	5.7	2.1	2.09	0.22	0.19	1.47	1.54	2.5	2.69
7	Watts (1998)—2*d*	♠		4.5	4.6	1.6	1.46	0.13	0.12	1.43	1.52	2.6	2.79
8	Watts (1998)—2*e*	♠		6.0	5.5	1.8	1.68	0.1	0.09	1.5	1.60	2.8	3.02
9	Watts (1998)—2*l*	♠		7.0	6.9	1.9	1.72	0.08	0.075	1.63	1.81	3.1	3.48
10	Grilli et al. (2002)	♠		5.2	5.2	2.0	1.95	1.17	1.19	2.12	2.09	1.9	1.81
11	Enet et al. (2003)	♠		4.5	4.5	1.2	1.13	0.44	0.45	0.7	1.16	1.4	1.42
12	Grilli and Watts (2005)—*a*		♠	2.6	2.6	1.4	1.53	1	1.17	1.8	1.96	1.6	1.59
13	Grilli and Watts (2005)—*b*		♠	8.0	8.0	4	4.23	1.1	1.37	2.1	2.45	2	2.17
14	Grilli and Watts (2005)—*c*		♠	16.0	16.0	6.5	8.08	1.4	1.47	2.5	2.71	2.2	2.49
15	Grilli and Watts (2005)—*d*		♠	20.5	21.0	8.5	9.94	1.4	1.56	2.75	2.96	2.7	2.8

Table 10
Verification of presented forecasting equations, far-field characteristics

No.	References	Status		x_P (mm)	Far-field leading wave characteristics									
					a_t (mm)		a'_c (mm)		a_c (mm)		t_{at} (s)		T_P (s)	
		L	N		Measured	Predicted	Measured	Predicted	Measured	Predicted	Measured	Predicted	Measured	Predicted
1	Rzadkiewicz et al. (1997)	♠		3000	90	96	56	58.9	25	27	15	15.38	4	4.17
2	Watts (1998)—2*n*	♠		252.9	9.8	8.99	3	3.23	2.8	2.94	0.85	1	0.4	0.39
3	Watts (1998)—2*n*	♠		505.8	6.8	7.83	2.8	2.96	2.2	2.04	1.25	1.36	0.37	0.43
4	Grilli et al. (2002)	♠		300	11	13.52	3.2	3.13	3	3.3	0.95	0.89	2.25	2.2
5	Grilli et al. (2002)	♠		600	12	11.77	4	4.5	3.4	3.6	1.2	1.19	2.2	2.39
6	Grilli et al. (2002)	♠		900	12.1	10.85	5	5.34	3.6	3.63	1.5	1.42	2.15	2.51
7	Grilli and Watts (2005)—*a*		♠	2832	6.1	5.71	3.1	3.49	1.8	1.83	1.9	1.76	2.2	2.54
8	Grilli and Watts (2005)—*b*		♠	2832	20	19.54	14	13.05	6.5	6	2.6	2.61	3.5	3.85
9	Grilli and Watts (2005)—*c*		♠	2832	33	40.96	23	22.84	10.2	9.9	3.1	3.12	4.3	4.63
10	Grilli and Watts (2005)—*d*		♠	2832	48	54.6	34	34.95	13	14.4	3.7	3.63	5.2	5.42

evaluate the present prediction formula in various conditions. It shall be considered that there is no any prediction equation or method in previous works for far-field characteristics of submarine-landslide generated waves. The prediction method for near-field characteristics is also limited as wave trough amplitude and period (Watts, 1998; Watts et al., 2005). As it can be seen in Tables 9 and 10, the comparison with previous data is made in a wide range of effective parameters. For instant, for the main effective parameters, bed slope and initial submergence, the variation range is 15 to 45°and 1 to 60 cm, respectively. For a detailed evaluation of prediction error, based on laboratory data which were obtained in our experimental work as well as the available experimental and numerical data in literature, the expected errors of each prediction equation are calculated and given in Table 11.

5. Conclusions

Laboratory investigations have been performed on the impulse waves caused by underwater landslide. 120 sets of details data have been measured in these experiments and the data sets are available on http://civil.sharif.edu/~ataie/ImpWave/SubmarinExp. The data sets can be a very useful data resource for other researchers either for theoretical analysis or for numerical model validation. Both rigid and deforming-slide masses were considered. The effects of the main parameters such as bed slope, initial submergence, slide geometry, shape and deformation on the impulse wave characteristics have been inspected.

Laboratory data analysis shows that the maximum water surface depression in underwater induced waves is strongly affected by bed slope angle, landslide initial submergence, thickness, and kinematics and weakly by landslide length, shape and deformation. Wave amplitude has a maximum reduction about 15% and period has a maximum increasing as 10% due to slide deformation. But the impulse wave feature at the near-field was not strongly different from impulse wave caused by rigid slide. Effects of slide shape on impulse wave feature were also investigated and it was concluded that the wave was affected strongly by the main geometric parameters of slide such as maximum thickness and total length parallel to the bed slope.

Recorded data at far-field wave gauges showed a leading low-amplitude positive wave which followed by a noticeable water surface depression as a trough, followed by a lower-order crest, and finally a wave train with decreasing amplitude and increasing period.

The energy conversion from landslide into the generated waves was also studied. The parameters which have the main role in energy conversion are sliding bed slope angle and initial submergence of blocks. The energy conversion was generally increased where the initial submergence of landslide decreases. Energy conversion in mild slopes was generally greater than steeper slopes. The slide deformation can make a maximum depression about 10% in energy conversion

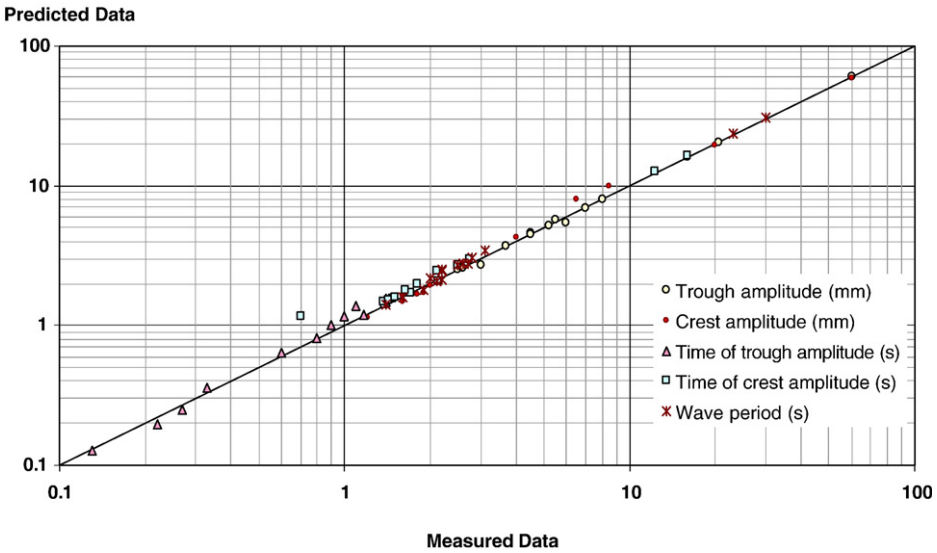

Fig. 17. Verification of presented forecasting equations, near-field wave characteristics.

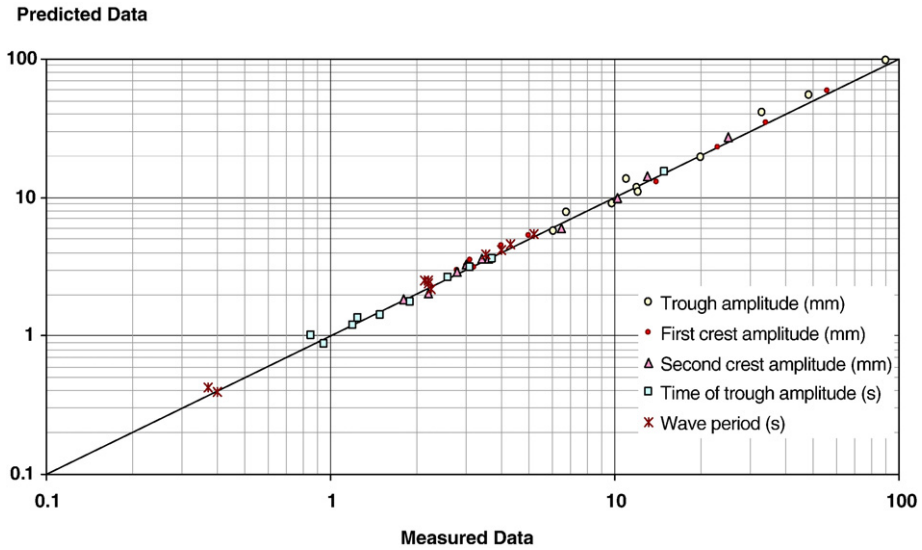

Fig. 18. Verification of presented forecasting equations, far-field wave characteristics.

ratio for cohesive and 20% for granular material slide. The variation of impulse wave energy during propagation into the wave tank was also investigated. The best-fit equations were presented for the maximum energy and its distance from the source.

The impulse wave nonlinearity at the generation zone was also examined. Measured impulse waves were generally nonlinear except for small amplitude waves observed in deeper sliding or in very mild bed slopes. The effective parameters on the impulse wave nonlinearity are initial submergence of slide, sliding bed slope angle, slide thickness, and still water depth.

Finally, prediction equations were presented for the estimation of impulse wave characteristics in near and far-field. The forecasting equations have been successfully verified using the available numerical and laboratory data in previously published works.

Acknowledgments

The financial support of the Water Resources Management Organization, Ministry of Power of the Islamic Republic of Iran is appreciated (Project number: DAM1-84010). Financial assistance was also provided partly by the Research Office of Sharif University of Technology, Iran. The contribution of the Marine Industries Laboratory of the Mechanical Department of Sharif University of Technology is also appreciated.

References

Ataie-Ashtiani, B., Najafi-Jilani, A., 2006. Prediction of submerged landslide generated waves in dam reservoirs: an applied approach. Dam Eng. XVII (3), 135–155 (November).
Ataie-Ashtiani, B., Najafi-Jilani, A., 2007. A higher-order Boussinesq-type model with moving bottom boundary: applications to submarine landslide tsunami waves. Int. J. Numer. Methods Fluids 53 (6), 1019–1048.
Ataie-Ashtiani, B., Malek-Mohammadi, S., 2007. Near field amplitude of sub-aerial landslide generated waves in dam reservoirs. Dam Eng. XVII (4), 197–222 (February/March).
Ataie-Ashtiani, B., Shobeyri, G., 2008. Numerical simulation of landslide impulsive waves by incompressible smoothed particle hydrodynamics. Int. J. Numer. Methods Fluids 56 (2), 209–232.
Dean, R.G., Dalrymple, R.A., 1991. Water wave mechanics for engineers and scientists. Advanced Series on Ocean Engineering, vol. 2. World Scientific, Singapore.
Enet, F., Grilli, S.T., Watts, P., 2003. Laboratory experiments for tsunami generated by underwater landslides: comparison with numerical modeling. In Proc. 13th Intl. Conf. on Offshore and Polar Engineering, Honolulu, Hawaii, USA, pp. 372–379 (May).
Fritz, H.M., Hager, W.H., Minor, H.E., 2004. Near field characteristics of landslide generated impulse waves. J. Waterw. Port Coast. Ocean Eng. 130, 287–302.
Grilli, S.T., Watts, P., 2005. Tsunami generation by submarine mass failure. I: modeling, experimental validation, and sensitivity analyses. J. Waterw. Port Coast. Ocean Eng. 283–297 (November/December).
Grilli, S.T., Vogelmann, S., Watts, P., 2002. Development of a 3D numerical wave tank for modeling tsunami generation by under water landslides. J. Eng. Anal. Bound. Elem. 26, 301–313.
Heinrich, P., 1992. Nonlinear water waves generated by submarine and aerial landslides. J. Waterw. Port Coast. Ocean Eng. 118, 249–266.
Johnson, J.W., Bermel, K.J., 1949. Impulsive waves in shallow water as generated by falling weights. Trans. Am. Geophys. Union 30, 223–230.
Kamphuis, J.W., Bowering, R.J., 1972. Impulse Waves Generated by Landslides. Proc. 12th Coastal Eng. Conf., vol. 1, pp. 575–588.

Table 11
Expected errors of prediction equations for impulse wave characteristics, the definition sketch of wave characteristics are shown in Fig. 7 for near-field and Fig. 11 for far-field

Wave stage	Equation no.	Predicted characteristic	Symbol	Expected error of predicted values	
				Based on this work	Based on available data
Near-field	(16)	Trough amplitude	a_{t1}	±2%	±8%
	(7)	Crest amplitude	a_{c1}	±4%	±11%
	(8)	Time of trough amplitude	t_{at1}	±6%	±15%
	(9)	Wave period	T_1	±6%	±15%
	(10)	Time of crest amplitude	t_{ac1}	±6%	±15%
Far-field	(11)	Trough amplitude	a_t	±7%	±12%
	(12)	First crest amplitude	a'_c	±8%	±13%
	(13)	Second crest amplitude	a_c	±8%	±13%
	(14)	time of trough amplitude	t_{at}	±10%	±15%
	(15)	Wave period	T_p	±10%	±15%

Lighthill, J., 1978. Waves in Fluids. Cambridge University Press, Cambridge, U.K.
Lynett, P., Liu, P.L., 2002. A numerical study of submarine-landslide-generated waves and run-up. Philos. Trans. R. Soc. Lond., U.K. A458, 2885–2910.
Najafi-Jilani, A., Ataie-Ashtiani, B., 2008. Estimation of near field characteristics of tsunami generation by submarine landslide. Ocean Eng. 35 (5–6), 545–557.
Panizzo, A., Girolamo, P.D., Risio, M.D., Maistri, A., Petaccia, A., 2005. Great landslide events in Italian artificial reservoirs. J. Natural Hazards Earth Syst. Sci. 5, 733–740.
Prins, J.E., 1958. Characteristics of waves generated by a local disturbance. Trans. Am. Geophys. Union 39 (5), 865–874.
Rzadkiewicz, S.A., Mariotti, C., Heinrich, P., 1997. Numerical simulation of submarine landslides and their hydraulic effects. J. Waterw. Port Coast. Ocean Eng. 149–157 (July/August).
Walder, J.S., Watts, P., Sorensen, O.E., Janssen, K., 2003. Tsunami generated by sub arial mass flows. J. Geophys. Res. 108 (B5), 2236 (EPM 2:1–2:19).
Watts, P., 1998. Wave maker curves for tsunami generated by underwater landslide. J. Waterw. Port Coast. Ocean Eng. 12 (3), 127–137.
Watts, P., Grilli, S.T., Kirby, J.T., Fryer, G.F., Tappin, D.R., 2003. Landslide tsunami case studies using a Boussinesq model and a fully nonlinear tsunami generation model. J. Natural Hazards Earth Syst. Sci. 3, 391–402.
Watts, P., Grilli, S.T., Tappin, D.R., Fryer, G.J., 2005. Tsunami generation by submarine mass failure. II: predictive equations and case studies. J. Waterw. Port Coast. Ocean Eng. 283–297 (November/December).
Wiegel, R.L., 1955. Laboratory studies of gravity waves generated by the movement of a submarine body. Trans. Am. Geophys. Union 36, 759–774.

Glossary

The following symbols are used in this manuscript:

α: landslide acceleration along the bed slope [LT^{-2}];
α_0: initial acceleration of slide mass [LT^{-2}];
γ: landslide special mass [$MT^{-2}L^{-2}$];
θ: sliding bed slope angle [deg.];
ζ: water surface displacement [L]
a_c: second crest amplitude of leading wave in propagation stage [L];
a_{c1}: initial impulse wave crest amplitude [L];
a'_c: first crest amplitude of leading wave in propagation stage [L];
a_t: trough amplitude of leading wave in propagation stage [L];
a_{t1}: initial impulse wave trough amplitude [L];
B: length of slide mass along the bed slope [L];
C_{c1}: initial impulse wave crest celerity [LT^{-1}];
C_{t1}: initial impulse wave trough celerity [LT^{-1}];
g: acceleration due to gravity [LT^{-2}];
h_0: still water depth in wave tank [L];
h_{0c}: initial submergence of mass center point for underwater slide [L];
S: location of mass center of block parallel to the inclined bed [L];
S_0: characteristic length-scale parameter of landslide kinematics [L];
t: time [T];
t_0: characteristic time of landslide motion [T];
t_{ac}: corresponding time of leading wave second crest [L];
t_{ac1}: corresponding time of initial impulse wave crest amplitude [T];
t'_{ac}: corresponding time of leading wave first crest [L];
t_{at}: corresponding time of leading wave trough [T];
t_{at1}: corresponding time of initial impulse wave trough amplitude [T];
t_b: beginning time of leading wave in recorded time series [L];
T: maximum thickness of the slide mass [L];
T_1: characteristic period of initial impulse wave [T];
T_p: characteristic leading wave period in propagation stage [L];
u: landslide velocity along the bed slope [LT^{-1}];
u_t: terminal velocity of slide mass [LT^{-1}];
V: landslide volume [L^3];
W: landslide mass [M];
x: horizontal coordinate [L];
x_p: propagation distance of impulse wave from source point [L]; and
z: vertical coordinate [L].